OXFORD

Hybridization of Alkali Basaltic Magmas: a Case Study of the Ogol Lavas from the Laetoli Area, Crater Highlands (Tanzania)

Anatoly N. Zaitsev[1,2]*, **Andrei A. Arzamastsev**[3,4], **Michael A. W. Marks**[5], **Simon Braunger**[5], **Thomas Wenzel**[5], **John Spratt**[2], **Tobias Salge**[2] and **Gregor Markl**[5]

[1]Department of Mineralogy, St Petersburg State University, University Emb. 7/9, St Petersburg 199034, Russia; [2]Department of Earth Sciences, Imaging and Analysis Centre, Natural History Museum, Cromwell Road, London SW7 5BD, UK; [3]Department of Petrography, St Petersburg State University, University Emb. 7/9, St Petersburg 199034, Russia; [4]Institute of Precambrian Geology and Geochronology, Russian Academy of Sciences, Makarova Emb. 2, St Petersburg 199034, Russia; [5]Universität Tübingen, Mathematisch-Naturwissenschaftliche Fakultät, FB Geowissenschaften, Schnarrenbergstrasse 94–96, Tübingen D-72076, Germany

*Corresponding author. Telephone: +7 812 3636221. E-mail: a.zaitsev@spbu.ru

ABSTRACT

The southern part of the eastern branch of the East African Rift is characterized by extensive volcanic activity since the late Miocene. In the Crater Highlands, part of the North Tanzanian Divergence zone, effusive and pyroclastic rocks reflect nephelinitic and basaltic compositions that formed between 4·6 and 0·8 Ma. The former are best represented by the Sadiman volcano (4·6–4·0 Ma) and the latter occur in the giant Ngorongoro crater (2·3–2·0 Ma), the Lemagarut volcano (2·4–2·2 Ma) and as a small volcanic field in the Laetoli area (2·3 Ma), where basaltic rocks known as Ogol lavas were erupted through fissures and several cinder cones. Compositionally, they are alkaline basalts with 46·0–47·9 wt% SiO_2, 3·0–4·3 wt% of $Na_2O + K_2O$, Mg# of 61 to 55, and high Cr and Ni content (450–975 and 165–222 ppm respectively). Detailed textural and compositional analysis of the major minerals (olivine, clinopyroxene, plagioclase and spinel-group minerals) reveals the heterogeneity of the rocks. The primary mineral assemblage that crystallized from the Ogol magmas comprises macro- and microcrysts of olivine ($Fo_{89.5-84.2}$), Cr-bearing diopside to augite, magnesiochromite–chromite$_{ss}$, magnetite–ulvöspinel$_{ss}$, andesine–oligoclase$_{ss}$ and fluorapatite, with glass of phonolitic composition in the groundmass. All samples contain appreciable proportions of xenocrystic minerals of macro- and microcryst size, with large variations in both concentration and mineral populations between samples. Xenocrysts include olivine with reverse zonation ($Fo_{84.1-72.5}$), rounded and embayed clinopyroxene cores of variable composition, anhedral Cr-free magnetite–ulvöspinel$_{ss}$ and embayed oligoclase. These xenocrysts as well as variations in major and trace element contents, $^{87}Sr/^{86}Sr_{(i)}$ (0·70377–0·70470) and $^{143}Nd/^{144}Nd_{(i)}$ (0·51246–0·51261) ratios provide evidence of multi-stage magma mixing and mingling between Ogol and adjacent Lemagarut volcano basaltic melts with only very minor contamination by Precambrian granite–gneisses. Elevated alkalinity of Ogol lavas, which positively correlates with isotope ratios, and the presence of xenocrystic green core clinopyroxene, perovskite, schorlomite and titanite indicate additional mixing and mingling with evolved nephelinitic magmas and/or assimilation of nephelinitic Laetolil tuffs or foiditic rocks related to the Sadiman volcano. Owing to their heterogeneity, estimates on the crystallization conditions for the Ogol rocks are difficult. Nevertheless, clinopyroxene–liquid thermobarometry indicates crystallization temperatures of around 1150–1220 °C and records upper-crustal depths of 3–12 km (1–4 kbar). Despite the fact that Ogol basalts are hybrid rocks that formed under open-system conditions with well-documented mixing and mingling

processes, they seem to be the best examples closest to primary basaltic melts within the Crater Highlands.

Key words: basalt; Crater Highlands; Laetoli; magma mixing and mingling; xenocryst

INTRODUCTION

Petrological studies during recent decades have provided plenty of evidence of magma hybridization in different tectonic environments, making this process very important in the observed compositional variability of igneous rocks (Sparks & Marshall, 1986; Blundy & Sparks, 1992; Perugini & Poli, 2012; Kokfelt et al., 2015; Morgavi et al., 2019, and references therein). Chemical mixing (or magma mixing) and mechanical mixing (mingling) are typical of magmatic provinces comprising numerous juxtaposed volcanic centers that operated within a relatively short time span (Clarke & Le Bas, 1990; Simonetti & Bell, 1993; Simonetti et al., 1996; Reubi et al., 2002; Mangler et al., 2020; Sundermeyer et al., 2020). In continental rifts developed in ancient cratonic zones, this process can be combined with significant assimilation of crustal material (e.g. Vladimirov et al., 2017).

The eastern branch of the East African Rift (EAR) opened along the border of the Tanzanian craton. It is known as a region of intense volcanism developed from late Miocene to Recent (see the recent reviews by Rooney, 2017, 2020a, 2020b, 2020c, 2020d). The volcanic rocks in this area include large volumes of plateau basalts and phonolites, compositionally variable stratovolcanoes (basalts to nephelinites, phonolites and trachytes, sometimes carbonatites), and numerous small explosion craters and cones that form monogenetic volcanic fields of variable composition.

Particularly interesting are volcanic complexes in the so-called North Tanzanian Divergence zone (NTD; Fig. 1; Baker et al., 1972) where volcanic activity started at around 6 Ma and continues to the present day at the active Oldoinyo Lengai volcano (Dawson, 2008; Mana et al., 2015). The main source of magmatism in the NTD is probably the metasomatized subcontinental lithospheric mantle (Mana et al., 2015), but the composition of potential primary melts remains unclear. Recent nephelinite–phonolite volcanic activity in the Lake Natron–Engaruka area may be related to primary olivine melilitite magma (Keller et al., 2006), but the alkali basalt–trachybasalt–trachyandesite–trachyte series documented from the Lemagarut, Ngorongoro and Oldeani volcanoes cannot be easily explained by fractionation of such parental melts.

Nearly all magma derivatives within the NTD exhibit geochemical and isotope signatures that indicate variable amounts of (1) mixing between mantle-derived melts from different sources (HIMU and EM1), and (2) crustal contamination (e.g. Bell & Dawson, 1995; Paslick et al., 1995; Bell & Tilton, 2001; Mollel, 2007; Dawson, 2008; Nonnote, 2007; Mana et al., 2015). Only few publications (e.g. Paslick et al., 1996) provide textural and mineralogical evidence to support such models, although the identification of different mineral populations (autocrysts–antecrysts–xenocrysts), their compositional zonation and their composition are extremely important for sound genetic interpretations of magma hybridization (mixing and mingling) processes, particularly in small-volume foidites and basanites (Duda & Schmincke, 1985), basalts (Dobosi, 1989; Dobosi & Fodor, 1992; Jankovics et al., 2016), nephelinites (Simonetti et al., 1996) and lamprophyres (Ubide et al., 2014).

The object of this study is a suite of the mafic Ogol lavas erupted within the Laetoli area of the Crater Highlands (northern Tanzania). Apart from multiphase volcanic edifices, these smaller cinder cone melts bypassed shallow magma reservoirs, thus sampling more primitive inputs that offer a window into the roots of the magma plumbing system (e.g. Carmichael et al., 2006; Corsaro et al., 2009; Petrone, 2010; Mangler et al., 2020). Mineralogy and geochemistry (including radiogenic Sr and Nd isotopes) of Ogol lavas are used to constrain their origin, depth of melting and source region character. We integrate these results with evolutionary paths of basalt–trachyte series in adjacent volcanoes and finally evaluate the role of possible magma mixing or mingling and crustal contamination.

GEOLOGICAL SETTING

Regional geology

The Crater Highlands and adjacent Gregory Rift are parts of the EAR, extending from the Afar triple junction southwards to the Mozambique margin along the western and eastern borders of the Tanzanian Craton, including numerous complexes in Ethiopia, Kenya and Tanzania. The NTD zone at the southern end of the southerly propagating eastern branch of the EAR is the focus of intense interaction of tectonic and magmatic processes along the margin of the Neoarchean Tanzanian Craton and the Proterozoic Mozambique belt (Smith, 1994; Plasman et al., 2019; Rooney, 2020a, 2020b, 2020c, 2020d) (Fig. 1). Intense volcanic manifestations within the north–south-trending Gregory Rift terminated at the craton margin and southward strain propagation expressed in numerous faults and lineaments (Le Gall et al., 2008). The eastward trend of the NTD zone is marked by the Essimingor–Meru–Kilimanjaro edifices, and further traced by the Chuilu Hills. The western upland zone is formed by volcanic
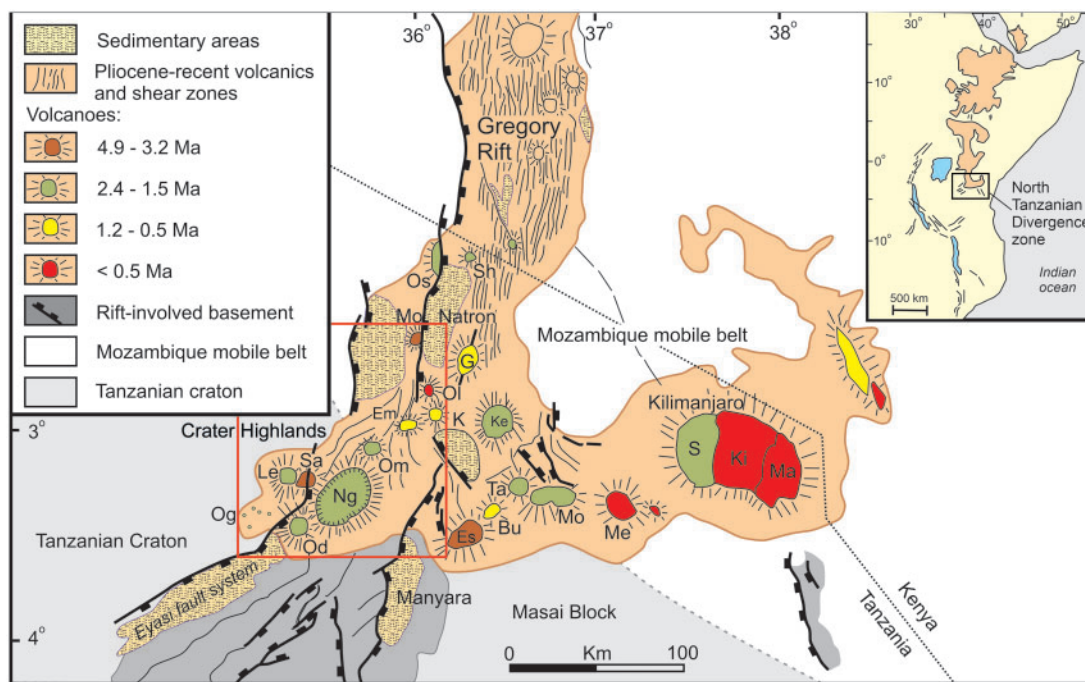
Fig. 1. Main structural and magmatic features in the North Tanzania Divergence zone (modified from Le Gall *et al.*, 2008). Volcanoes: Bu, Burko; Em, Embagai; Es, Essimingor; G, Gelai; K, Kerimasi; Ke, Ketumbeine; Ki, Kibo; Le, Lemagarut; Mo, Monduli; Ma, Mawenzi; Me, Meru; Mo, Mosonik; Ng, Ngorongoro; Od, Oldeani; Og, Ogol; Om, Olmoti; Os, Oldoinyo Shira; Ol, Oldonyo Lengai; S, Shira; Sa, Sadiman; Sh, Shombole; Ta, Tarosero. The red rectangle shows the Crater Highlands area and corresponds to the digital elevaion model image in Fig. 2. Age data are from Mollel (2007), Dawson (2008, and references therein), Nonnotte *et al.* (2008), Mana *et al.* (2012, 2015) and Peirce & Mana (2018).

centers of the Crater Highlands. Geochronological and petrographic data provide no clear evidence for a regular distribution of volcanic centers within the NTD zone. However, a recent study (Mana *et al.*, 2015) provides evidence of consistent younging of NTD magmatism along two main trends: one from west to east (Essimingor to Kilimanjaro) and another from SW to NE (Sadiman to Gelai).

The earliest manifestation of volcanic activity is represented by an alkali picrite–nephelinite–phonolite series from Essimingor volcano dated to 5.91 ± 0.02 Ma (Mana *et al.*, 2012). Further alkaline magma eruptions throughout the NTD zone formed Sadiman, Mosonik, Engelosin, Tarosero and other minor centers ranging in age from 4.6 to 2.3 Ma (Dawson, 2008). Silica undersaturated alkaline magma eruptions were replaced and superimposed by Lemagarut, Ngorongoro, Monduli, Olduvai, Olmoti and Oldeani volcanoes, calderas and minor centers in which basalts and basanites are the predominant rock types. Vast basalt lava beds spread along the southern end of Gregory Rift in the Engaruka–Manyara area.

Based on $^{40}Ar/^{39}Ar$ age determinations, basaltic magmatism in the NTD zone lasted from 2.4 Ma to 1.6 Ma (Manega, 1993; Foster *et al.*, 1997; Mollel, 2007). Since 1.3 Ma renewal of magmatism was marked by continuing activity in the axial part of the NTD, and its lateral eastward spreading. Alkaline rocks ranging in composition from primitive olivine melilitite to highly evolved phonolite, sporadically associated with carbonatite, form

the Embagai, Burko, Kerimasi, Meru and Oldoinyo Lengai volcanoes and numerous minor craters and cones in the Lake Natron–Engaruka area (Dawson, 2008; Mattsson *et al.*, 2013).

In multiphase volcanic centers, such as Kilimanjaro and Ketumbeine, early mafic magmatism started at 2.2 Ma (simultaneously with Ngorongoro and other basaltic centers) followed by phonolitic eruptions dated to 1.3 and 0.5 Ma, respectively (Nonnotte *et al.*, 2008; Peirce & Mana, 2018).

Crater Highlands

The Crater Highlands comprise numerous eruptive centers in a 100 km long elevated area between lakes Natron and Eyasi at the southern termination of the eastern branch of the EAR (Fig. 2). Seismic tomography reveals a thick mantle keel (exceeding 200 km) beneath the craton (Ritsema *et al.*, 1998; Adams *et al.*, 2012), considerably thicker than the lithosphere beneath the Eastern Rift north of Lake Natron, which is less than 100 km thick (Birt *et al.*, 1997). Although the contact between Archaean and Late Proterozoic crust is west of the Crater Highlands (Plasman *et al.*, 2019), outcrops of gneissic–granitic basement indicate that Archaean lithosphere underlies much of this rift sector. Recent local magnetotelluric and tomography studies (Plasman *et al.*, 2019) indicate the presence of a melt accumulation zone at 40 km depth below the Crater Highlands, potentially connected to the volcanic edifices at the
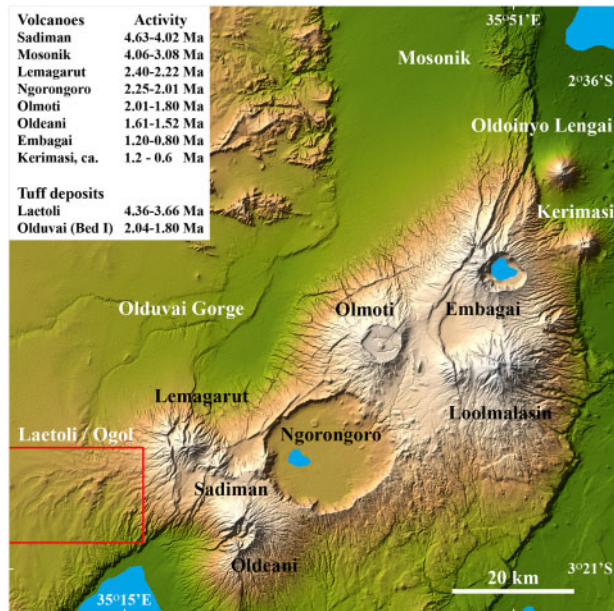
Fig. 2. Major volcanoes and tuff deposits in the Crater Highlands (shaded and coloured SRTM elevation model, February 2000). Courtesy NASA/JPL-Caltech. The red rectangle shows the studied area and corresponds to the geological map on Fig. 3. Age data are from Mollel (2007), Dawson (2008) and Deino (2011, 2012).

surface. The Eyasi fault system, which delimits the westward distribution of magmatism in the upland area, is interpreted as a narrow vertical conduit linking the surface to a deeper conductive structure between two large basement terrains (Plasman *et al.*, 2019).

The earliest volcanic activity, beginning at 4.63 ± 0.05 Ma (Mollel *et al.*, 2011), produced large volumes of interlayered phonolitic tuffs, tuff breccias and nephelinitic lava flows erupted from Sadiman volcano (Zaitsev *et al.*, 2011, 2012). Superimposed tuffs west of Sadiman, in particular the Laetolil Footprint Tuff, where 3.66 Ma *Australopithecus afarensis* footprints were discovered (Leakey & Hay, 1979), may have been erupted from Mosonik volcano (Zaitsev *et al.*, 2015, 2019). Since about 2.4 Ma, mafic magmatism predominates in the Crater Highlands. Eruptions from the Lemagarut volcano occurred between 2.40 ± 0.01 and 2.22 ± 0.10 Ma and the giant Ngorongoro volcano was active between 2.25 ± 0.02 and 2.01 ± 0.02 Ma (Mollel *et al.*, 2008, 2011), erupting basalts, basanites and their evolved derivatives (trachyandesite, trachydacite and trachyte). The youngest manifestations of mafic magmatism are represented by the Oldeani volcano, which was active between 1.61 ± 0.01 and 1.52 ± 0.02 Ma (Mollel, 2007).

Ogol lavas
Basaltic lavas (local name Ogol lavas) erupted through fissures and cinder cones ranging from 0.5 to 1.5 km in diameter and from 50 to 150 m in height (Hay, 1987; Supplementary Data Fig. S1; supplementary data are available for downloading at http://www.petrology. oxfordjournals.org). The major localities (as named on

Quarter degree sheet 52 Endulen; Pickering, 1964) are Oldoinyo Mati (Ndonyamati), Oldoinyo Emusenge (Norsigidok), Oldoinyo Ildolaunya (Ndolanya) and Oldoinyo Naisiusiu hills (Fig. 3). Outcrops with well-exposed lava flows are limited, but rounded lava blocks up to 2.5 m in diameter are widespread (Supplementary Data Fig. S1). The Ogol lavas are massive (common) to vesicular (rare), fine- to medium-grained, and have aphanitic (rare) to porphyritic (common) textures. The proportions of phenocrysts (olivine and pyroxene) are highly variable and range from *c*. 1 to 30 vol. % (Supplementary Data Fig. S2). The Ogol lavas overlie the Laetolil (4.36–3.66 Ma) and Ndolanya (3.58–2.66 Ma) beds and are partly overlain by the 2.15–2.06 Ma Naibadad beds (Hay, 1987; Deino, 2011) and by basalts and basaltic andesites of the Lemagarut volcano. Mollel (2007) reported two $^{40}Ar/^{39}Ar$ ages (2.31 ± 0.01 and 2.27 ± 0.05 Ma) collected from the NE-trending Ogol lava flow west of Lemagarut volcano.

Despite their importance for the understanding of basaltic volcanism in the Crater Highlands (Mollel, 2007) as well as in anthropological studies in Laetoli (Adelsberger *et al.*, 2011), the Ogol lavas are poorly studied. They were originally described as vogesites (Hay, 1987) and subsequently classified as basalts (Mg# = 49–59) with olivine and augite as phenocrysts, and plagioclase, augite and Ti-rich magnetite as groundmass phases (Mollel, 2007). Although study by Mollel (2007) provided high-precision ages (see above), geochemical and mineralogical data are limited and incomplete. A more extensive geochemical study was published by Adelsberger *et al.* (2011). Based on whole-rock data, the rocks were classified as basalts and basanites with one sample each of tephrite and picrobasalt. The basaltic and some of the basanitic samples are relatively primitive (Mg# of 55–61) with appreciable Cr (496–1091 ppm) and Ni (188–248 ppm).

SAMPLES AND METHODS
For this study we investigated 15 samples of Ogol lavas and 12 samples of lavas from the western part of the Lemagarut volcano (Fig. 3). Crystalline basement rocks are not exposed in the Laetoli area, but at the Eyasi plateau about 15 km south and SW from the Laetoli area. We collected eight samples from basement rocks of the Tanzania craton, comprising granite–gneisses, green and melanocratic schists and garnet amphibolites with an age of about 2.7 Ga (Supplementary Data Table S1; Pickering, 1964; Fletcher *et al.*, 2018).

Mineral identification was based on petrographic and scanning electron microscopy studies of polished thin sections [Leica DM 2500P microscope and Hitachi S-3400N scanning electron microscope (SEM), St Petersburg State University]. X-ray powder diffraction (XRD) data for the 15 Ogol samples were collected using a D2Phaser (Bruker) diffractometer, CoKα_{1+2} radiation with $\lambda_{CoK\alpha1} = 1.78900$ Å and $\lambda_{CoK\alpha2} = 1.79283$ Å, 2theta = 5–85°, operated at 30 kV and 10 mA (St
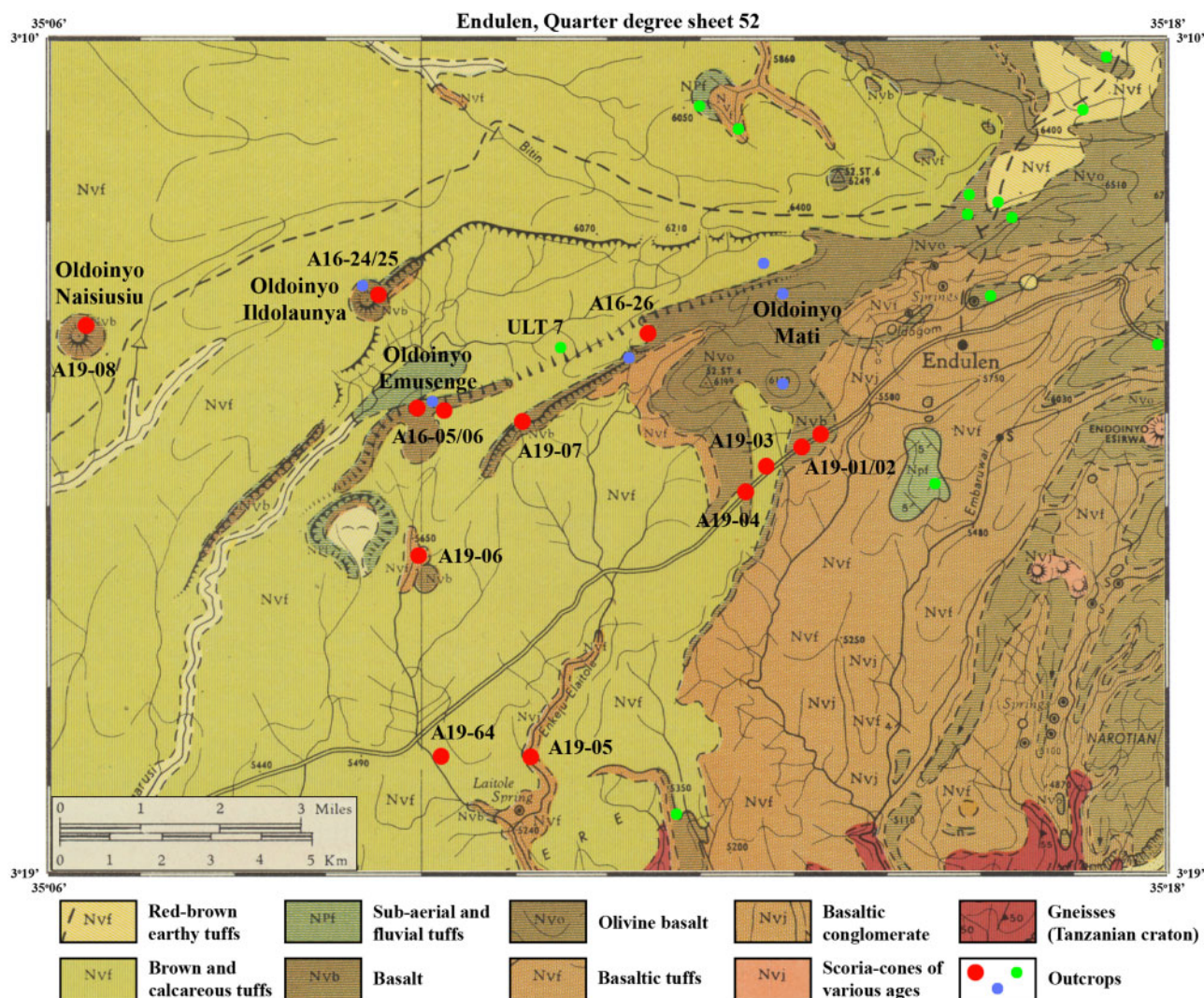
Fig. 3. Cropped Quarter Degree Sheet 52 Endulen (Pickering, 1964) showing geology of the Laetoli area (red rectangle in Fig. 2). Major outcrops with Ogol basalts are shown by red dots (this study) and blue dots (Mollel, 2007; Adelsberger *et al.*, 2011); green dots are outcrops with Lemagarut basalts, Laetolil tuffs (ULT 7, Upper Laetoli Tuff 7 with *Australopithecus afarensis* footprints) and tuffs with nephelinite xenoliths (likely to be derived from Sadiman).

Petersburg State University). Mineral identification was performed by matching of powder XRD patterns with the ICDD database records. Quantitative phase analysis of four samples was carried out by full-profile Rietveld refinement using a Bruker TOPAS v.5.0 software.

Mineral compositions (olivine, clinopyroxene, spinel and plagioclase) were obtained by electron microprobe analysis (wavelength-dispersive X-ray spectrometry (WDS) mode) using a JEOL 8900 Superprobe (Tübingen University) and Cameca SX-100 (Natural History Museum, London) instruments operated at same analytical conditions (20 kV, 20 nA with a beam diameter of 1 μm for olivine, clinopyroxene and spinel, and 10 μm for plagioclase); well-characterized natural and synthetic compounds were used for calibration (see Supplementary Data Table S2 for a compilation of the WDS configurations, standards and detection limits). The accuracy of the analyses were controlled by permanent test measurements on standard minerals with

known compositions. The k-ratios were generally in the range $0.99 < x < 1.01$. The standard deviation is used to characterize the precision of the data as a 'relative error', and is $<1\%$ for major elements, and mostly $<5\%$ for minor elements (up to 20 % for elements close to detection limits). Glass composition was obtained by using a Hitachi S-3400N scanning electron microscope (St Petersburg State University) equipped with an Oxford Instruments X-Max 20 spectrometer [energy-dispersive spectrometry (EDS); Table 5; 20 kV, 1·0 nA and defocused beam 10–15 μm in diameter].

Energy-dispersive spectrometry was performed using a Zeiss EVO LS15 SEM and a Zeiss Ultra plus field emission SEM (The Natural History Museum, London). Large area elemental maps were obtained with an Oxford Instruments Aztec EDS system and an XMax 80 mm² silicon drift detector. An accelerating voltage of 20 kV and a beam current of ~6 nA resulted in an EDS input count rate ~260 000 counts per second. EDS

spectra were acquired with a dwell time of 2.5 ms and stored as hyperspectral imaging datasets at a resolution of 128×92 pixels per field, corresponding to a pixel size of $\sim3\,\mu m$. Backscattered electron (BSE) images were acquired at a resolution of 256×192 pixels, corresponding to a pixel size of $\sim1.5\,\mu m$. Each thin section was analysed by 1102–1647 fields. Aztec software was used to stitch the individual fields into one hyperspectral imaging dataset with an EDS resolution up to 16 megapixels. The distribution of elements is displayed as net intensity maps where the background has been subtracted and peaks with overlapping X-ray lines have been deconvolved.

Whole-rock samples (lavas and basement rocks, Table 1, Supplementary Data Table S1) were analysed for major and trace elements by X-ray fluorescence (XRF) and inductively coupled plasma mass-spectrometry (ICP-MS) at the Karelian Research Centre RAS (Petrozavodsk). Powders were fused into glass disks using *c.* 3 g of sample mixed with lithium tetraborate ($Li_2B_4O_7$). Glass disks were analyzed by XRF using an ARL ADVANT"X X-ray sequential fluorescence spectrometer. The uncertainties were 0.7–5 % for elements with concentrations of >0.5 wt% and up to 12 % for elements with concentrations of <0.5 wt%. The concentrations of trace elements were determined by ICP-MS using an X Series 2 instrument. Powdered samples were digested in acid mixture in open vessels following the standard procedure described by Svetov *et al.* (2015). The accuracy of the analyses was monitored by simultaneous digestion and analysis of USGS reference materials BHVO-2 and BIR-1a, and in-house SGD-2a (GSO 8670-2005) reference material (Vasil'eva & Shabanova, 2017*a*, 2017*b*) (Supplementary Data Table S1). The relative standard deviation (RSD) is generally 1–5 %, 7 % for Th and 11 % for Ta (Supplementary Data Table S1). Loss on ignition (LOI) was determined gravimetrically.

The Rb–Sr and Sm–Nd isotopic compositions of the 10 Ogol samples, three Lemagarut samples, and three basement rock samples were analysed using a multi-collector Triton mass spectrometer operated in static mode (VSEGEI, St Petersburg). A powdered sample was blended with weighed amounts of mixed ^{149}Sm–^{150}Nd and ^{87}Rb–^{84}Sr spike solutions. Then the prepared sample was dissolved in a mixture of nitric and hydrofluoric acids. Rb and Sr were separated for isotope analysis using cation exchange chromatography with AG50W-X8 resin. Sm and Nd were separated for isotope analysis in two stages. The first stage included the separation of all rare earth elements (REE) from the bulk of the sample using cation exchange chromatography with AG50W-X8 resin. The second stage included extraction chromatography using a liquid HDEHP on Teflon carrier as a cation exchange medium. A correction for Nd isotope fractionation was introduced using the normalization of the measured values to $^{146}Nd/^{144}Nd = 0.7219$. The normalized ratios were adjusted to $^{143}Nd/^{144}Nd = 0.511860$ in the La Jolla Nd

isotope standard. A correction for Sr isotope fractionation was introduced using the normalization of the measured values to $^{86}Sr/^{88}Sr = 0.1194$. The normalized ratios were adjusted to $^{87}Sr/^{86}Sr = 0.710250$ in the SRM-987 Sr isotope standard. The errors for the determined Sm, Nd, Rb and Sr contents were 0.5 %. The Sm and Nd blanks were 10 and 20 pg, respectively. The Rb and Sr blanks were 30 pg each. The analysis of the BCR-1 standard yielded the following values (mean of 10 measurements): 6.45 ppm Sm, 28.4 ppm Nd, $^{147}Sm/^{144}Nd = 0.1382 \pm 3$, and $^{143}Nd/^{144}Nd = 0.512656 \pm 8$; 45.9 ppm Rb, 329 ppm Sr, $^{87}Rb/^{86}Sr = 0.4023 \pm 9$, $^{87}Sr/^{86}Sr = 0.705013 \pm 16$.

WHOLE-ROCK GEOCHEMISTRY

Whole-rock geochemical data for 13 Ogol samples are given in Table 1. The studied samples have relatively low SiO_2 (46.0–47.9 wt%) and $Na_2O + K_2O$ (3.0–4.3 wt%) contents, and are rich in MgO (8.8–11.7 wt%), CaO (10.0–12.3 wt%) and Fe_2O_{3total} (13.2–15.5 wt%), with Mg# values [calculated as $100Mg/(Mg + 0.9Fe_{total})$] ranging from 61 to 55. In a total alkali vs SiO_2 (TAS) diagram (Le Bas *et al.*, 1986) most Ogol samples plot in the alkaline basalt field (Fig. 4a). For further comparison and discussion, we use published (Mollel, 2007; Nonnotte, 2007; Mollel *et al.*, 2008; Adelsberger *et al.*, 2011) and our unpublished data from adjacent Lemagarut volcano and Ngorongoro caldera that are relevant to evaluating 2.4–2.2 Ma magmatism in the Crater Highlands. Data from the nearby located but older nephelinitic Sadiman volcano (Zaitsev *et al.*, 2012) are also considered as they are important for later discussion on mineralogy of the basalts (see below).

The Ogol basalts are not compositionally uniform; in particular, a suite of three samples is high in TiO_2 (4.1–4.2 wt%) and low in MgO (7.6–8.0 wt%) (Adelsberger *et al.*, 2011). Another high-Ti rock was described as picrobasalt with low Si (40.3 wt% SiO_2) and Mg (3.4 wt% MgO) and unusually high P (2.1 wt% P_2O_5) contents (Adelsberger *et al.*, 2011). High-Ti basalts occur only at Ngorongoro (up to 4.1 wt% TiO_2), but were not found at Laetoli or Lemagarut during this and previous studies (Nonnotte, 2007; Mollel, 2007; Mollel *et al.* 2008; authors' unpublished data). If these samples were collected from boulder-sized blocks, which are extremely abundant at Laetoli, they are most probably related to eruptions of the giant Ngorongoro volcano.

Overall, there are negative correlations between the contents of MgO and SiO_2, Al_2O_3, Na_2O, K_2O and P_2O_5 (Fig. 4b and c) and less evident positive correlations of MgO with Fe_2O_3 and CaO. The contents of compatible elements, such as Cr and Ni, are variable and high, with 297–1091 ppm and 77–248 ppm, respectively (Fig. 4d). The lowest Cr (297–338 ppm) and Ni (77–95 ppm) contents are observed in high Ti and low Mg–Si basalt (Adelsberger *et al.*, 2011).

Table 1: Whole-rock geochemical data for the studied Ogol basalts

Sample:	A16-05	A16-06	A16-25	A16-26	A19-01	A19-02	A19-06	A19-07	A19-08	A19-64	A19-4c	A19-4b
Latitude	741 220	740 683	739 808	745 223	748 761	748 497	740 867	742 655	734 090	741 124	747 201	747 201
Longitude	9 642 114	9 642 261	9 644 377	9 643 513	9 641 516	9 641 340	9 639 339	9 641 864	9 643 749	9 635 170	9 640 489	9 640 489
wt%												
SiO_2	45.90	45.16	46.19	45.60	46.68	44.95	45.03	46.31	46.68	47.27	46.61	47.12
TiO_2	3.06	3.54	2.99	2.98	2.80	2.77	3.37	3.01	2.75	2.70	2.85	2.86
Al_2O_3	7.59	8.45	10.00	8.99	9.44	9.61	8.94	9.96	9.85	10.13	10.16	10.00
Fe_2O_{3total}	14.37	15.45	13.72	14.07	13.79	13.47	14.53	13.90	13.17	13.44	13.47	13.23
MnO	0.18	0.19	0.18	0.19	0.17	0.18	0.19	0.18	0.18	0.18	0.21	0.18
MgO	11.50	10.97	8.54	9.58	10.22	10.46	9.42	9.60	9.36	8.82	9.15	9.24
CaO	12.32	11.23	10.82	12.13	11.30	9.98	12.04	10.81	11.03	10.35	10.98	11.04
Na_2O	2.27	1.90	2.81	2.19	2.16	2.97	2.09	2.76	2.67	2.62	2.80	2.89
K_2O	1.06	1.00	1.37	1.25	1.11	1.20	1.16	1.35	1.30	1.19	1.44	1.37
P_2O_5	0.34	0.41	0.43	0.39	0.39	0.39	0.40	0.41	0.45	0.38	0.49	0.50
S_{total}		0.03	0.09	0.05		0.02	0.01	0.02	0.02	0.01		0.02
LOI	0.89	1.36	2.36	2.14	1.48	3.66	2.25	1.22	2.09	2.53	1.29	1.02
Total	99.48	99.69	99.50	99.56	99.54	99.66	99.43	99.53	99.55	99.62	99.45	99.47
Mg#	61	58	55	57	59	61	56	58	58	57	57	58
ppm												
Li	7.60	7.21	6.98	8.21	7.19	7.35	9.13	8.34	9.05	9.55	11.32	9.57
Sc	36.3	25.7	26.7	27.0	29.5	30.1	28.9	28.0	27.8	29.1	29.3	30.3
V	293	266	205	232	257	251	280	245	228	214	238	245
Cr	975	519	497	542	479	450	520	450	458	520	572	569
Co	78.4	57.4	53.7	55.9	70.0	60.3	64.9	61.1	58.9	62.9	63.2	64.2
Ni	222	197	171	183	183	165	190	174	172	185	196	198
Cu	190	143	138	139	147	166	169	143	152	138	175	189
Zn	118	105	114	106	110	109	114	112	107	118	111	120
Ga	15.2	13.0	17.7	14.7	16.6	13.5	18.3	15.0	14.8	16.1	15.2	16.1
Rb	20.1	15.8	22.8	19.5	21.2	20.6	20.3	23.7	13.7	17.5	25.3	22.6
Sr	560	608	846	757	614	924	665	765	733	855	827	842
Y	19.1	19.2	21.6	19.5	19.7	18.6	19.7	20.7	20.2	20.2	22.2	22.8
Zr	194	186	362	358	179	192	198	208	203	202	218	233
Nb	50.5	47.8	59.2	52.5	53.8	52.8	54.6	60.4	62.8	58.0	66.1	69.1
Cs	0.15	0.18	1.42	0.13	0.22	0.13	0.14	0.16	0.31	0.13	0.20	0.27
Ba	781	362	910	854	622	658	987	1076	732	638	979	1130
La	38.2	42.7	52.1	47.5	47.3	47.2	45.8	52.3	54.1	46.9	59.2	60.9
Ce	86.9	84.6	99.9	89.6	88.7	93.5	94.1	104	105	93.5	119	119
Pr	10.2	10.9	12.1	11.1	11.2	10.7	11.0	11.7	11.8	10.7	13.1	13.1
Nd	41.8	44.6	48.6	44.5	41.9	42.6	44.0	46.5	45.9	41.1	51.6	50.8
Sm	8.43	9.24	9.51	9.01	8.19	8.25	8.84	8.87	8.77	8.05	9.52	9.67
Eu	2.50	2.53	2.86	2.61	2.32	2.43	2.57	2.68	2.65	2.42	2.90	2.88
Gd	7.04	7.48	7.90	7.25	6.88	6.82	7.11	7.28	7.10	6.70	7.81	7.73
Tb	0.96	0.98	1.02	0.95	0.98	0.90	1.02	1.03	0.97	0.95	1.07	1.07
Dy	4.74	4.93	5.38	4.82	4.69	4.70	4.95	4.91	4.96	4.64	5.17	5.27
Ho	0.88	0.81	0.86	0.79	0.85	0.90	0.90	0.94	0.96	0.88	1.06	1.00
Er	1.97	2.15	2.36	2.11	2.01	2.00	2.09	2.18	2.07	2.07	2.24	2.21
Tm	0.27	0.25	0.30	0.25	0.27	0.29	0.29	0.31	0.30	0.30	0.31	0.32
Yb	1.54	1.59	1.87	1.58	1.67	1.63	1.66	1.76	1.70	1.72	1.82	1.75
Lu	0.20	0.21	0.25	0.21	0.20	0.21	0.21	0.23	0.23	0.22	0.25	0.24
Hf	5.29	5.42	9.41	9.30	5.51	4.96	5.56	5.58	5.29	5.03	5.49	5.58
Ta	2.99	3.25	3.55	3.25	2.96	3.24	3.24	3.63	3.60	3.26	3.80	3.72
Pb	5.03	4.82	4.01	5.07	4.81	5.00	4.71	5.49	5.48	4.69	6.59	5.77
Th	5.08	5.27	6.61	5.89	5.50	6.21	5.64	6.76	7.18	6.01	7.69	7.48
U	0.89	1.05	1.46	0.85	1.12	1.27	0.85	0.97	1.38	1.23	0.84	0.89

LOI, loss on ignition. Mg# = $100Mg/(Mg + 0.9Fe_{total})$. Map datum WGS84, latitude and longitude in UTM coordinate system, zone 36M. Major elements were determined by XRF and trace elements were determined by ICP-MS (for details see section 'Samples and methods').
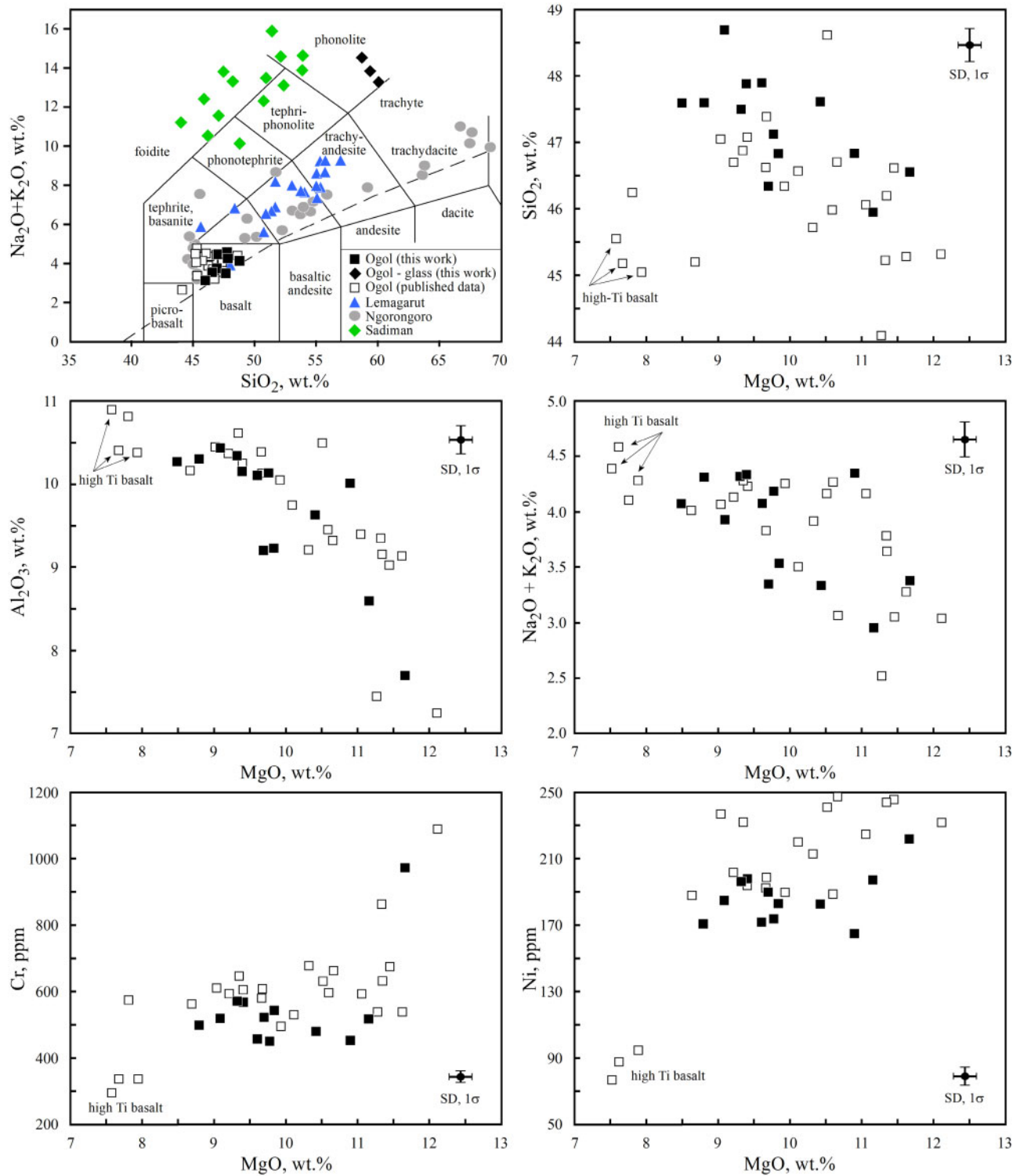
Fig. 4. Compositional variations for the Ogol basalts. (a) Total alkali vs SiO$_2$ diagram (TAS; Le Bas *et al.*, 1986). The dashed line divides alkaline and tholeiitic basalts. Compositions of basaltic series from the Lemagarut and Ngorongoro volcanoes and nephelinites from the Sadiman volcano are shown for comparison. (b–f) Major and compatible element variations (for the Ogol basalts only). Three samples of high-Ti basalts are probably not related to the Ogol basalts (see the section 'Whole-rock geochemistry'). Published data are from Mollel (2007), Nonnotte (2007), Adelsberger *et al.* (2011), Mollel *et al.* (2011) and Zaitsev *et al.* (2012).

The Ogol lavas are broadly enriched in incompatible trace elements with respect to the primitive mantle and are characterized by slightly positive Ba and Pb anomalies and negative U, K and P anomalies (Fig. 5a); some samples display marked positive Zr and Hf anomalies. The contents of REE range from 206 to 276 ppm (Table 1) and there is a tendency of increasing REE content with decreasing MgO. Chondrite-normalized REE patterns are

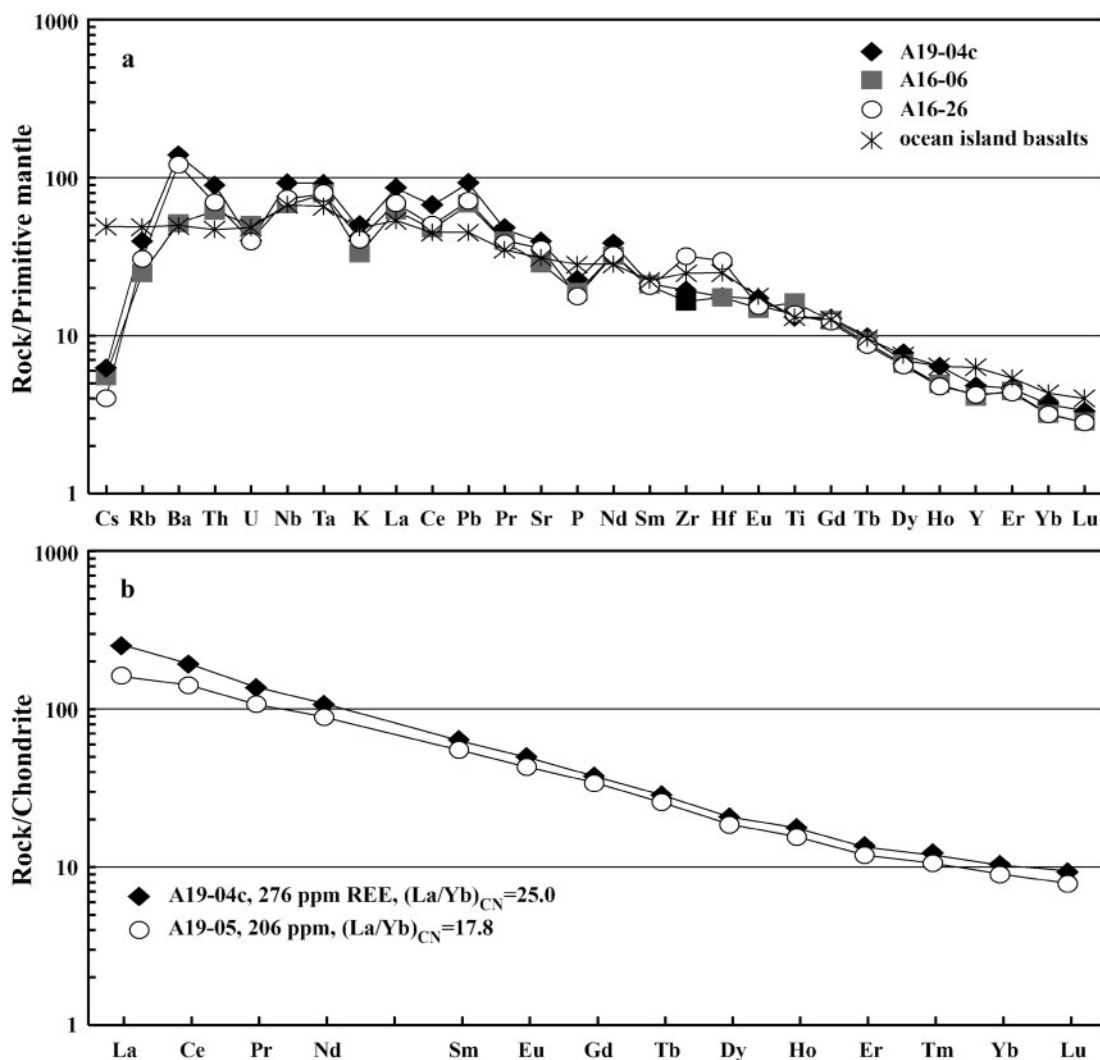**Fig. 5.** Primitive mantle- and chondrite-normalized plots for selected Ogol basalt samples. Data for ocean island basalts, and normalizing values for primary mantle and chondrite are from Sun & McDonough (1989). For Pb and Ce recommended normalizing values of 0·071 ppm and 0·0079 ppm respectively were used.

enriched in light REE (LREE) with $(La/Yb)_N$ ratios of 17·8–25·0 and $(La/Lu)_N$ ratios of 20·5–27·2 (Fig. 5b).

Considerable scatter in the major and trace element data of the studied samples argue against simple closed-system fractional crystallization or mixing between two hypothetic endmembers. The reasons for that will be understandable based on the following detailed petrographic descriptions and mineral chemical investigations.

PETROGRAPHY AND MINERAL CHEMISTRY

The studied Ogol samples are characterized by variable structures, textures and proportions of mineral crystals (Supplementary Data Fig. S2). In this study we prefer not to use the term 'pheno- and microphenocrysts', because, as recent studies showed, crystals in volcanic rocks commonly represent very complex mineral assemblages. They consist of autocrysts (or phenocrysts *sensu stricto*), primary minerals that are cogenetic with their host rock; antecrysts (crystals that crystallized from the same magmatic system, but have been recycled one or several times before inclusion in the specific sample); microlites (crystallized during degassing of magma on eruption); and xenocrysts that were entrained from other contaminant components (e.g. Jerram & Martin, 2008; Ubide *et al.*, 2014; Shane *et al.*, 2019). Therefore, the terms macro- and microcrysts will be used for petrographic description of the Ogol basalts.

The mineral contents are highly variable, with clinopyroxene (48–56 wt%), plagioclase (17–23 wt%) and olivine (9–13 wt%) as the dominant minerals and minor spinel-group minerals (6–8 wt%) and apatite (1–2·5 wt%) as determined via Rietveld refinement of the powder X-ray diffraction data (Rp, difference between observed and calculated patterns, is 3·6–3·9 %). The only macrocrysts (>500 μm) are olivine and clinopyroxene, with the latter being commonly more abundant (Fig. 6). They are generally 1–3 mm in size (rarely up to 5 mm on the
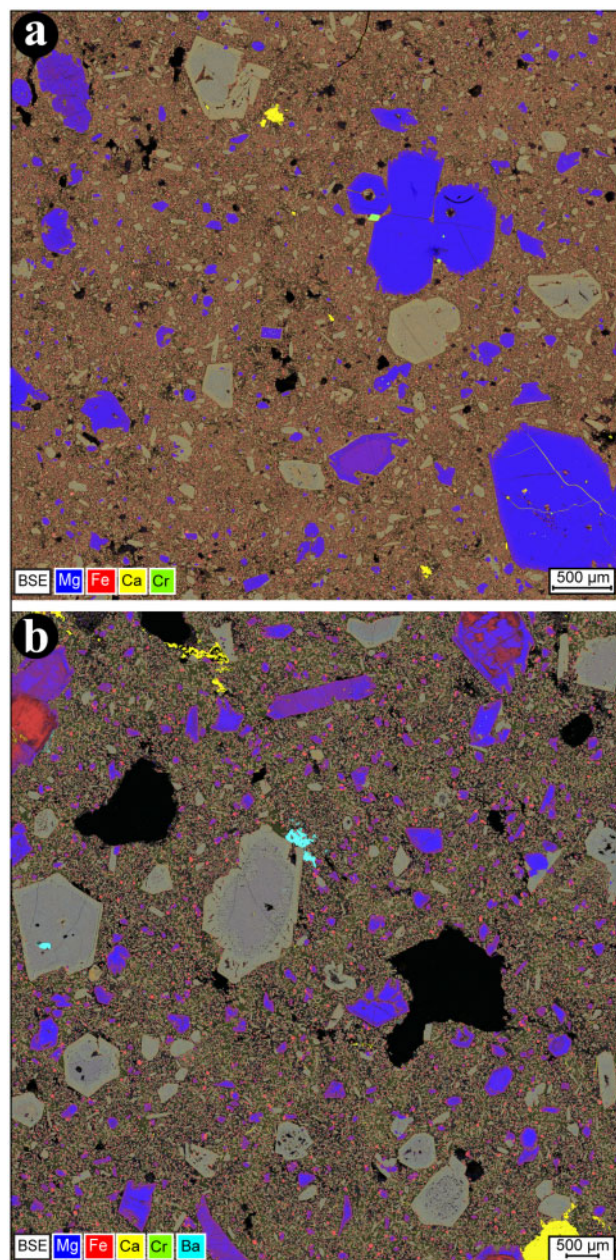
Fig. 6. Net intensity EDS composite elemental maps combined with BSE images of the Ogol basalts. (a) Sample A16-06, field of view 9·48 mm × 9·22 mm; blue, olivine; beige, clinopyroxene; light green, magnesiochromite; pink in groundmass, magnetite; yellow, calcite; black, holes; (b) sample A16-26, field of view 9·48 mm × 10·20 mm; blue, olivine; orange–brown, olivine alteration; beige to light violet–beige, clinopyroxene; orange–brown in groundmass, magnetite; yellow, calcite; turquoise, baryte; black, holes. Original resolution is 6778 × 6662 pixels (A16-06) and 6230 × 6677 pixels (A16-26).

longer axis), few of them reaching megacrystic size of 9 mm × 3 mm (olivine) and 9 mm × 8 mm (clinopyroxene). Microcrysts (100–500 μm) include olivine, clinopyroxene and rare plagioclase and spinel (not spinel *sensu stricto*, but spinel as a mineral group). Groundmass minerals (<100 μm) are olivine (rare), clinopyroxene, plagioclase and spinel. Textural data suggest the

presence of several populations of olivine, clinopyroxene and spinel. Macrocrysts, microcrysts and groundmass crystals are characterized by different morphologies, zonation patterns, internal structures and compositions.

Large area EDS elemental mapping of thin sections and blocks showed that apatite is relatively abundant in the groundmass, and rare pyrrhotite and chalcopyrite occur as inclusions in clinopyroxene. Previously, these minerals have not been found in the Ogol basalts (Mollel, 2007; Adelsberger *et al.*, 2011). Ilmenite was mentioned by Adelsberger *et al.* (2011) as a groundmass mineral; however, it was not identified by reflected light microscopy, SEM–EDS and XRD studies in our samples as a primary mineral (only ilmenite exsolution lamellae in magnetite were observed in one sample). As Adelsberger *et al.* (2011) did not describe (abundant) spinel-group minerals in Ogol basalts, we suggest that they may have mixed up ilmenite with spinel.

The majority of the studied samples show variable degrees of alteration and the most altered samples (A16-24 and A16-25) derive from Oldoinyo Ildolanya hill. Olivine is partly to fully replaced by fine-grained brown hydrous Mg–Fe-rich silicate (not precisely identified); calcite is a common secondary mineral and fills vesicles and forms veins and veinlets. SEM–EDS studies also indicate the presence of a montmorillonite, sodalite, Na–K feldspar and Na (± K) zeolite. This mineral assemblage is considered to be a result of glass alteration. Further secondary minerals include Sr-bearing baryte (veinlets and small nests), and rare Ba-bearing celestine, Ba–Mn hydroxide and dolomite (Fig. 6b). Exceptions are two samples from the Oldoinyo Emusenge hill (A16-05 and A16-06) that show only little alteration (Fig. 6a).

Olivine

Most olivine macrocrysts (and some of the larger microcrysts) are 'hopper crystals' (Fig. 7) but they also occur as euhedral to subhedral crystals, partly showing initial stages of skeletal growth at crystal edges (Fig. 7b and e). Few grains are subhedral to anhedral (Fig. 7g and f) and their morphology suggests that they represent fragments of broken crystals, showing a kink-banded texture. The overall compositional range (311 analyses from 10 samples) is $Fo_{89.5}$ to $Fo_{72.5}$ (Table 2, Fig. 8) and based on their internal structures and compositions, we distinguish five olivine populations:

with normal zonation (Mg-rich core with Fe-rich rim, abundant macrocrysts and rare microcrysts);
with reverse zonation (Fe-rich core with Mg-rich rim, abundant macrocrysts and rare microcrysts);
with repetitive zonation (Fe-rich core, Mg-rich mantle and Fe-rich rim, rare macrocrysts);
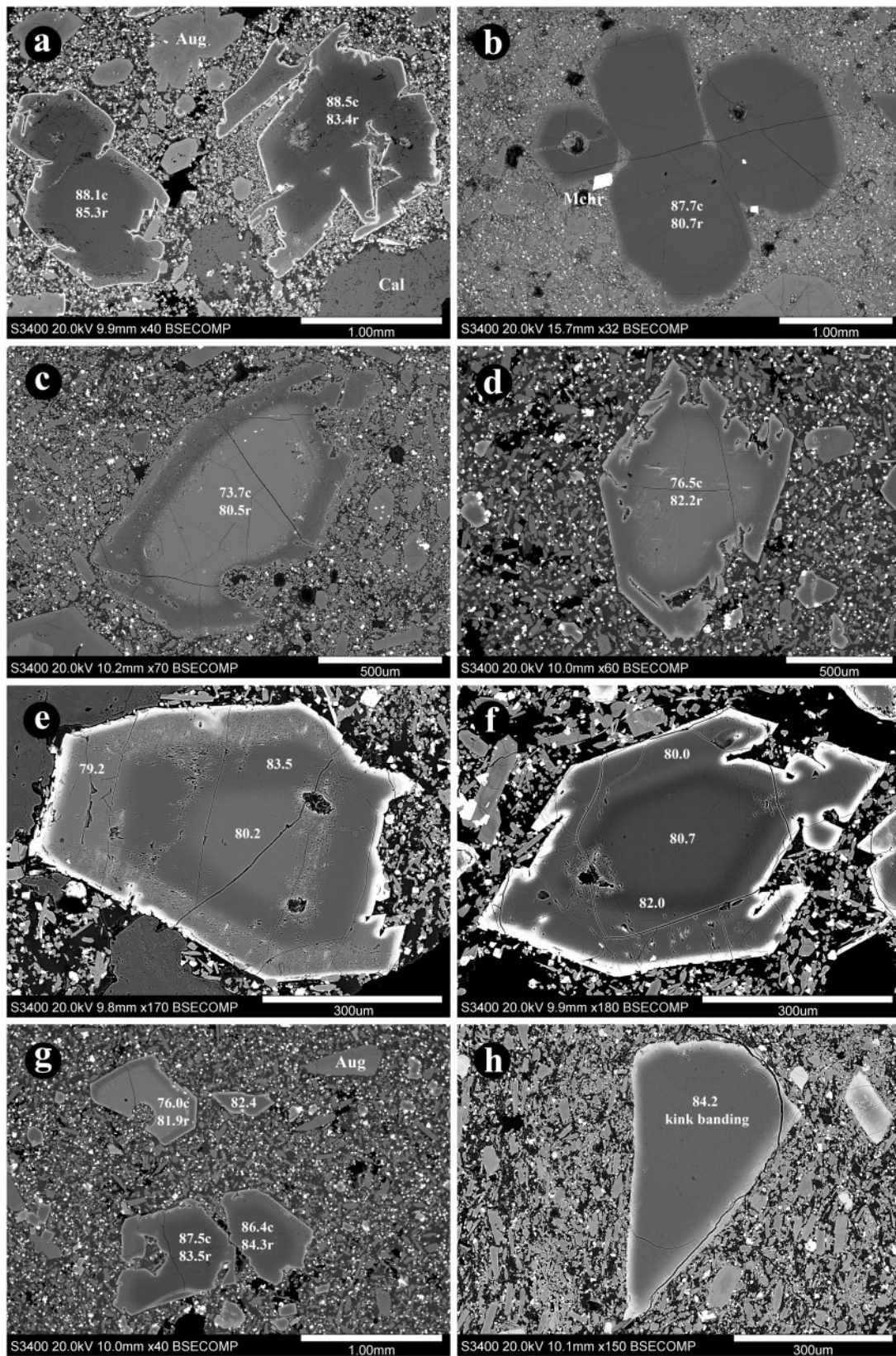with no zonation (abundant microcrysts and groundmass crystals);

Fig. 7. Olivine morphology and zonation (BSE images). (a) Hopper olivine with normal zonation, A19-06; (b) euhedral to subhedral olivine with normal zonation; Mchr, magnesiochromite, A16-05; (c) hopper olivine with reverse zonation, A16-05; (d) hopper olivine with reverse zonation, A19-07; (e) euhedral olivine with repetitive zonation, A19-01; (f) hopper olivine with repetitive zonation, A19-01; (g) olivine with normal zonation, fragment of olivine with reverse zonation and angular microcrysts (A19-07); (h) fragment of unzoned olivine, A19-08. Numbers are Fo values (mol%); c, core; r, rim.

Table 2: Selected compositions of olivine

Sample:	16-05					16-06		19-04c		16-05		16-06		19-07		16-06		19-08	
Zonation:	normal									reverse						unzoned			
Crystal:	pheno core	pheno core	rim	pheno core	rim	pheno core	rim	micro core	rim	pheno core	rim	pheno core	rim	pheno core	rim	micro core	gm core	fragment core	fragment core
Analysis:	26	7	9	3	5	18	20	150	151	16	19	14	19	71	73	52	13	139	145
SiO_2	41.60	41.13	40.02	40.61	39.64	40.65	40.10	41.42	40.53	38.23	39.68	38.38	39.53	39.72	40.26	39.65	39.65	40.83	39.41
TiO_2		0.03	0.03				0.03	0.03	0.03			0.03			0.03				
Al_2O_3		0.03	0.05						0.03			0.03						0.03	
FeO	9.25	9.93	15.95	10.99	17.38	13.22	15.26	12.95	17.26	24.65	16.29	23.42	17.66	19.93	17.28	15.69	17.23	16.19	21.49
MgO	48.62	48.23	43.05	48.37	43.42	45.73	44.03	45.72	42.35	37.50	44.00	38.26	43.02	40.13	42.38	44.63	43.32	43.49	38.66
MnO	0.16	0.15	0.30	0.13	0.25	0.19	0.23	0.20	0.33	0.30	0.21	0.26	0.23	0.32	0.32	0.21	0.23	0.18	0.29
CaO	0.31	0.34	0.42	0.34	0.36	0.29	0.25	0.33	0.31	0.27	0.37	0.27	0.34	0.17	0.34	0.31	0.38	0.26	0.25
NiO	0.33	0.28	0.17	0.33	0.20	0.23	0.22	0.35	0.25	0.05	0.21	0.14	0.20	0.13	0.21	0.25	0.19	0.20	0.11
Cr_2O_3	0.08	0.10	0.05	0.09	0.11	0.06	0.03	0.06	0.06						0.04	0.06			
Total	100.34	100.18	100.03	100.86	101.36	100.37	100.16	101.05	101.14	101.00	100.76	100.79	100.98	100.40	100.87	100.80	101.00	101.19	100.21
Si	1.013	1.007	1.009	0.994	0.995	1.008	1.007	1.018	1.016	0.996	0.996	0.996	0.996	1.015	1.012	0.993	0.997	1.016	1.017
Ti			0.001						0.001			0.001							
Al		0.001	0.001				0.001	0.001	0.001			0.001			0.001			0.001	
Total	1.013	1.008	1.011	0.994	0.995	1.008	1.008	1.019	1.018	0.996	0.996	0.998	0.996	1.015	1.013	0.993	0.997	1.017	1.017
Mg	1.765	1.761	1.619	1.766	1.624	1.691	1.648	1.675	1.582	1.456	1.647	1.480	1.617	1.529	1.589	1.666	1.624	1.614	1.487
Fe	0.188	0.203	0.336	0.225	0.365	0.274	0.320	0.266	0.362	0.537	0.342	0.508	0.372	0.426	0.363	0.329	0.362	0.337	0.464
Mn	0.003	0.003	0.006	0.003	0.005	0.004	0.005	0.004	0.007	0.007	0.004	0.006	0.005	0.007	0.007	0.004	0.005	0.004	0.006
Ca	0.008	0.009	0.011	0.009	0.010	0.008	0.007	0.009	0.008	0.008	0.010	0.008	0.009	0.005	0.009	0.008	0.010	0.007	0.007
Ni	0.006	0.006	0.003	0.006	0.004	0.005	0.005	0.007	0.005	0.001	0.004	0.003	0.004	0.003	0.004	0.005	0.004	0.004	0.002
Cr	0.002	0.002	0.001	0.002	0.002	0.001	0.001	0.001	0.001						0.001	0.001			
Total	1.973	1.984	1.977	2.010	2.010	1.983	1.986	1.962	1.965	2.008	2.008	2.005	2.007	1.969	1.973	2.014	2.006	1.966	1.966
Fo	89.5	88.8	81.9	87.8	80.8	85.3	83.0	85.4	80.5	72.5	82.0	73.8	80.5	77.6	80.5	82.7	81.0	82.1	75.6

Fo, forsterite end-member, mol%. WDS analysis (JEOL 8900 Superprobe).

with no zonation (rare crystal fragments of various size with kink-banded texture).

The proportion between normally and reversely zoned crystals is highly variable. In samples from Oldoinyo Emusenge (A16-05 and A16-06) reversely zoned olivine is extremely rare, in other samples normally zoned and reversely zoned olivine occurs in similar amounts, and in sample A19-64 reversely zoned olivine dominates. Olivine grains showing repetitive zonation are extremely rare, with only two crystals observed in one sample (A19-01). Subhedral to anhedral grains (unzoned or with partial rim) are less common, but abundant in a sample from Oldoinyo Naisiusiu (A19-08).

Normally zoned olivine has a core composition with $Fo_{89.5}$ to $Fo_{84.2}$ with NiO between 0·44 and 0·20 wt%. Both Fo and Ni contents decrease towards the rim with $Fo_{85.9-80.7}$ and 0·31–0·17 wt% NiO (Fig. 8). In reversely zoned olivine, the cores are variable in composition ($Fo_{72.5-84.1}$; 0·05–0·31 wt% NiO) and their rims are always higher in Fo ($Fo_{80.2-86.0}$) and NiO (0·18–0·32 wt%) (Fig. 8). A single olivine megacryst (sample A19-08) is compositionally similar to the cores in reversely zoned olivine, but it is normally zoned with a Fo- and Ni-rich core ($Fo_{79.2-77.6}$, 0·22–0·17 wt% NiO) and a Fo- and Ni-depleted rim ($Fo_{77.3-76.4}$; 0·15–0·14 wt% NiO). Microcryst and groundmass olivine has a composition similar to that of the rim on olivine crystals with both zonation types. Aphanitic samples (A19-04a, b and c) contain zoned microcrysts (which are very close to 500 μm in size) with core enriched in both Fo and NiO (e.g. $Fo_{86.6-85.4}$ and 0·36–0·33 wt% NiO). These values are similar to those for olivine cores in porphyritic basalt varieties. Two macrocrysts with repetitive zonation contain Fe-enriched core and rim with similar composition ($Fo_{79.2-80.7}$, 0·07–0·10 wt% NiO) and mantle that is slightly enriched in Mg ($Fo_{82.0-83.5}$, 0·18–0·23 wt% NiO). Subhedral to anhedral olivine fragments (with kink-banded texture) are generally rare, but abundant in one sample (A19-08; Fig. 7h). The composition of these fragments is highly variable ($Fo_{86.3-75.4}$; 0·32–0·10 wt% NiO; Fig. 8). In addition, minor Ca, Mn and traces of Cr were detected (Table 2) with generally high Ca and low Mn in high-Fo olivine and low Ca and high Mn in low-Fo olivine.

Clinopyroxene

Clinopyroxene occurs as euhedral to subhedral macrocrysts, microcrysts and groundmass crystals, with a single megacryst (Fig. 9, Supplementary Data Fig. S2). Compared with olivine, clinopyroxene occurs more often as fragments of broken crystals. Most clinopyroxene crystals are colourless, with a few crystals containing greenish cores. In some samples microcrysts define a trachytoid texture and rarely they occur as glomerocrysts. Based on variable shapes, zonation patterns, internal structures (Fig. 9), and compositions (Table 3; Figs. 10–12), we distinguish six populations of clinopyroxene. In total 342 spot analyses were obtained from 12 samples. Most analyses indicate diopsidic to augitic compositions, with rare hedenbergite and aegirine–augite compositions in greenish cores.

Population I (common) is represented by cores of euhedral to subhedral macro- and microcrysts (Fig. 9a, b, and d), typically not in optical continuity with the mantle or rim zones. These cores are characterized by a variable morphology (round, oval, embayed) and sometimes show strong resorption at their boundary with the mantle or rim. Their Mg# values [calculated as $100Mg/(Mg + Fe^{2+})$] and contents of Cr, Al and Ti point to three varieties (Ia, Ib and Ic; Table 3). Variety Ia is augite ($Di_{60-68}Hed_{12-16}others_{19-25}$) with Mg# between 85 and 80, low Cr (always below detection limit) and high Al (3·2–3·8 wt% Al_2O_3) and Ti (1·3–1·7 wt% TiO_2). Variety Ib ($Di_{51-63}Hed_{14-20}others_{22-33}$) has Mg# of 81–73, contains higher Cr (0·05–0·4 wt% Cr_2O_3) and high but variable Al and Ti (2·3–4·7 wt% Al_2O_3 and 0·6–1·6 wt% TiO_2). Variety Ic ($Di_{68-76}Hed_{6-11}others_{16-21}$), with high Mg# values of 94–87, is rather Cr-rich (0·4–1·4 wt% Cr_2O_3) but depleted in Al and Ti (0·3–0·5 wt% TiO_2 and 0·8–1·8 wt% Al_2O_3). Varieties Ia and Ic contain similar amounts of Na_2O (0·5–0·6 and 0·4–0·7 wt% respectively), whereas variety Ib is slightly enriched in Na (typically 0·7–1·0 wt% Na_2O, with two spot analysis of 0·5 wt%).

Population II (less common, but abundant in some samples) occurs as rounded and embayed cores in macrocrysts (Fig. 9c). A prominent feature is their large size, typically 1–4 mm and up to 9 mm × 8 mm, and their irregular extinction. Unlike population I, these crystals do not have a mantle zone. Augite ($Di_{60-75}Hed_{8-14}others_{16-29}$) has a relatively high Mg# (90–83) and contains elevated Cr (0·3–0·7 wt% Cr_2O_3). Other minor components are Al (1·3–2·9 wt% Al_2O_3), Ti (0·4–1·0 wt% TiO_2) and Na (0·5–0·7 wt% Na_2O) (Table 3).

Population III (common) is augite ($Di_{54-74}Hed_{10-21}others_{13-30}$) with a characteristic spongy texture (Fig. 9d and e) that occurs as cores in euhedral to subhedral macro- and microcrysts or as mantle around augite I. In the latter case it forms either complete or discontinuous mantle zone. The mineral has a variable Mg# (86–74), contains relatively little Cr (0·1–0·4 wt% Cr_2O_3 with one spot analysis of 0·8 wt%) and variable amounts of Al (1·6–4·0 wt% Al_2O_3), Ti (0·5–1·9 wt% TiO_2) and Na (0·3–0·9 wt% Na_2O) (Table 3).

Despite the observed compositional differences between augite I, II and III, there is a common feature for these three populations—a negative correlation between values of Mg# and content of Al and Ti (Figs 11 and 12). The behavior of Cr is different: augite with Mg# between 85 and 73 contains Cr at approximately similar and relatively low level, whereas high-Mg# augite (94–85) shows a positive correlation between Mg# and Cr.

Population IV (generally rare, but common in some samples) occurs as greenish cores in euhedral to subhedral microcrysts and rarely macrocrysts, typically not in optical continuity with the rim of the crystals (Fig. 9f
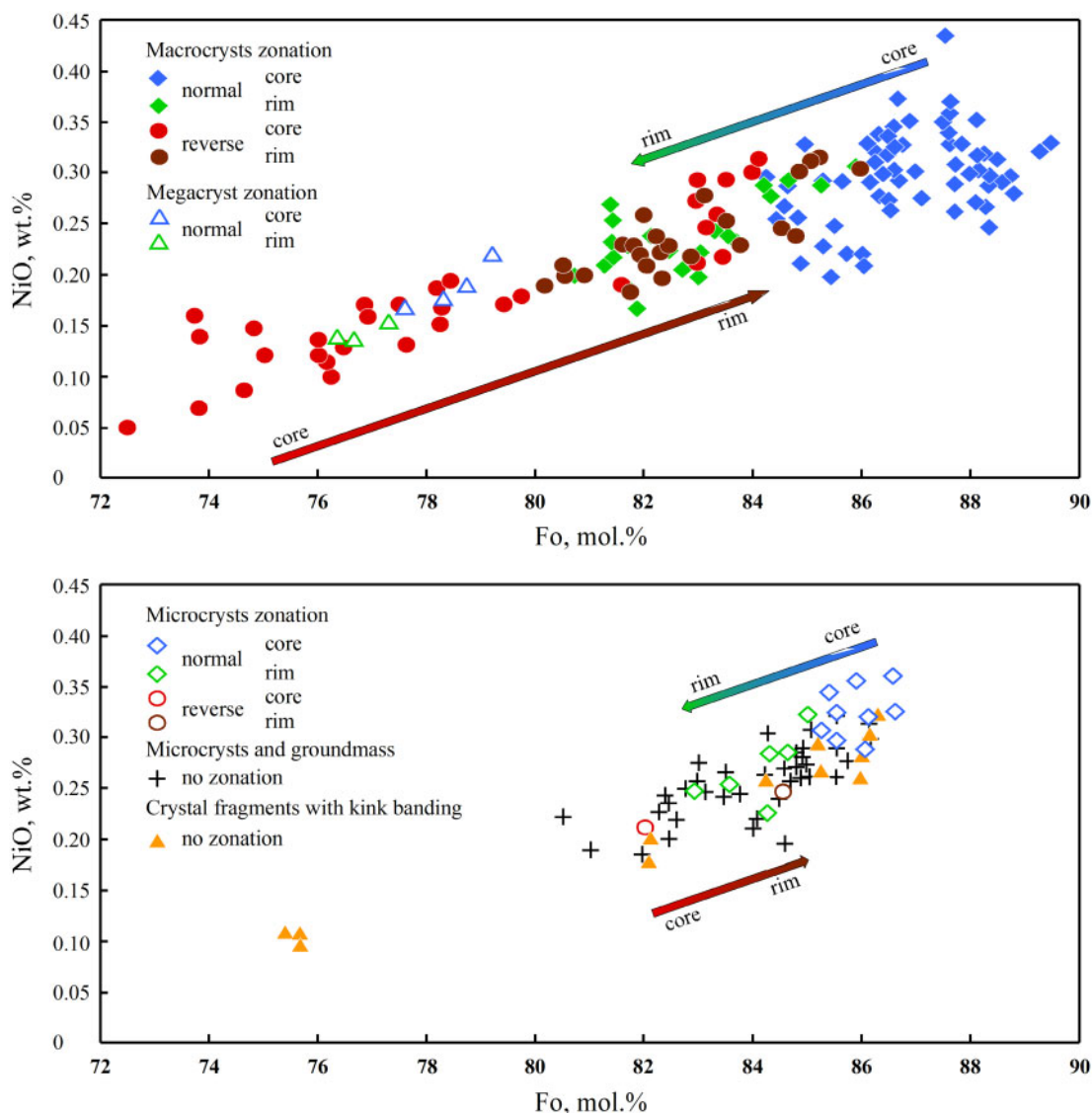
Fig. 8. Olivine composition, Fo (mol%) vs NiO (wt%) in the Ogol basalts. RSD_{Ni} varies between 2 and 7% dependent on the Ni content.

and g). Some of these cores contain inclusions of Ti-rich garnet (schorlomite), titanite and/or apatite (Fig. 9f). Clinopyroxene IV is compositionally very diverse ($Di_{18-76}Hed_{10-62}Aeg_{3-20}others_{2-23}$); minerals are characterized by a highly variable Mg# values (86–26) and Al, Ti and Na contents (0·4–5·1 wt% Al_2O_3, 0·3–2·2 wt% TiO_2 and 0·8–3·8 wt% Na_2O) (Table 3). The Cr contents are below the detection limit with the exception of one crystal (Fig. 9g) that contains 0·17–0·24 wt% Cr_2O_3. Also, this crystal contains a mantle zone whereas others do not.

Population V (common) occurs as two varieties. One occurs as mantles around cores of populations I, III and rarely IV (Fig. 9a, b, d, e, and g) and generally shows oscillatory zoning, with rare continuous growth zonation. Another represents euhedral to subhedral macrocrysts (rare), microcrysts (common) and groundmass (common) crystals with oscillatory-type or rarely sector-type zoning (Fig. 9h and i). This augite ($Di_{56-76}Hed_{6-21}others_{12-30}$) has high Mg# values with a range from 93

to 73 and high Cr contents (up to 1·4 wt% Cr_2O_3), which decrease towards the rims (Table 3, Fig. 10). In contrast, Al and Ti increase from the inner mantle–core (1·2 wt% Al_2O_3 and 0·4 wt% TiO_2) towards the outer mantle–rim (5·7 wt% Al_2O_3 and 3·6 wt% TiO_2). These compositional variations are related to the size of the crystals: macrocrysts have a core with higher Mg# values and lower Al–Ti contents compared with microcrysts and groundmass crystals, which have lower Mg# and higher Al–Ti contents. Variable Na (0·2–0·7 wt% Na_2O) correlates positively with Cr (Supplementary Data Fig. S3), suggesting a minor kosmochlor $NaCr(Si_2O_6)$ component (up to 4 mol%). However, molar Na/Cr ratio is always ≥1 (up to 9·2), suggesting that some of the Na is incorporated as aegirine and/or jadeite components (Supplementary Data Fig. S3).

Population VI (common) is augite ($Di_{49-69}Hed_{12-26}others_{14-29}$), which forms thin rims around almost all macrocrysts, microcrysts and groundmass crystals
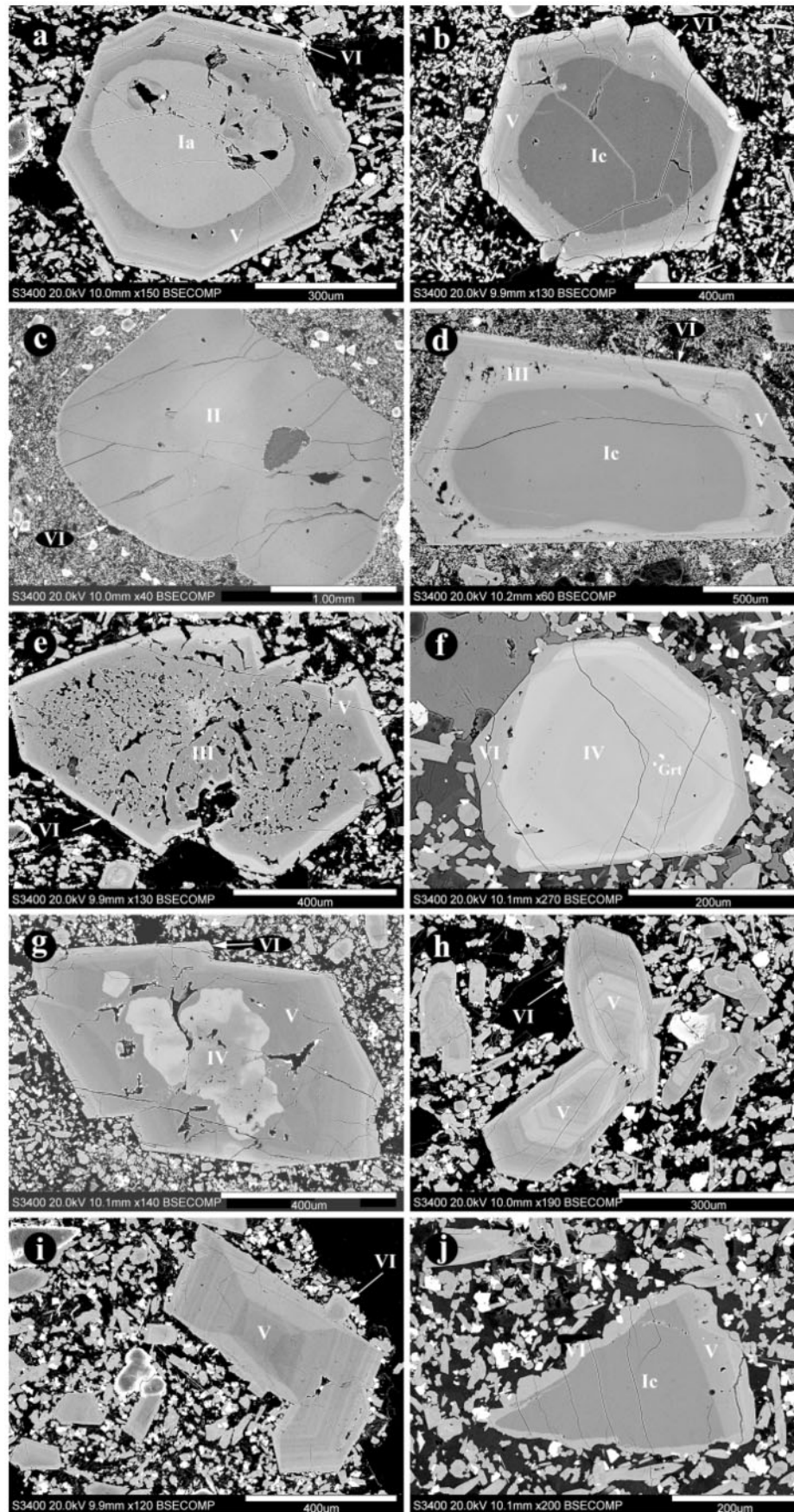
Fig. 9. Clinopyroxene morphology and zonation (BSE images). I–VI, clinopyroxene population; (a, e) sample A19-64, (b) A19-01, (c) A19-08, (d) A19-02, (f) A19-04a, (g) A16-06, (h) A19-06, (i) A16-05, (j) A19-04b. Crt, schorlomite.

Table 3: Selected analyses of clinopyroxene

Sample:	16-05	16-06	16-25	16-26	19-04a	16-06	19-04c	19-07	19-08	16-06	19-64	16-26		19-07	19-04a		19-08	16-06	16-06
Population:	Ia		Ib		Ic			II				III			IV				
Analysis:	26	31	43	33	1	49	113	97	123	134	3	102	53	110	14	6	125	21	23
SiO_2	50.19	49.32	51.33	53.41	53.89	53.44	54.62	53.68	54.32	52.90	54.19	50.99	53.18	52.88	51.58	47.61	51.69	50.74	50.76
TiO_2	1.67	1.57	1.30	0.63	0.51	0.42	0.42	0.64	0.50	0.84	0.43	1.93	0.83	0.93	0.52	1.99	0.51	0.95	0.97
Al_2O_3	3.34	3.82	4.00	2.35	1.81	1.05	1.32	2.50	1.85	2.56	1.30	3.23	2.30	2.14	1.26	5.10	0.69	3.36	3.40
Cr_2O_3			0.21	0.31	1.37	0.89	0.53	0.38	0.71	0.32	0.47	0.20	0.23	0.32				0.24	0.17
Fe_2O_3	3.03	4.36				2.29				0.41	0.24	0.16		0.78	3.33	4.44	6.32	4.06	3.54
FeO	5.31	4.36	8.65	6.68	3.54	2.22	4.01	5.57	4.63	5.72	3.60	7.77	6.53	4.52	10.93	8.15	14.07	6.46	4.50
MnO	0.17	0.21	0.18	0.13	0.09	0.09	0.10	0.11	0.10	0.13	0.09	0.18	0.12	0.11	0.45	0.31	0.80	0.29	0.17
MgO	14.20	13.97	13.69	16.16	17.14	18.06	18.28	17.08	17.42	15.88	18.23	13.41	15.60	16.18	8.42	8.75	4.46	12.52	15.36
NiO				0.03	0.09		0.05	0.04	0.05		0.08	0.04	0.03	0.03					
CaO	21.88	22.06	19.63	19.24	21.39	21.43	20.74	19.96	20.75	20.95	20.86	22.37	20.99	22.41	21.25	22.47	17.35	20.34	20.32
Na_2O	0.58	0.57	0.81	0.53	0.70	0.50	0.50	0.65	0.62	0.65	0.50	0.48	0.46	0.41	1.84	1.27	3.71	1.38	0.75
Total	100.37	100.25	99.80	99.47	100.52	100.39	100.57	100.61	100.95	100.36	100.00	100.76	100.26	100.73	99.58	100.08	99.60	100.34	99.94
Si	1.859	1.832	1.908	1.972	1.952	1.940	1.971	1.947	1.960	1.934	1.966	1.887	1.953	1.927	1.977	1.812	2.017	1.889	1.874
Al	0.141	0.167	0.092	0.028	0.048	0.045	0.029	0.053	0.040	0.066	0.034	0.113	0.047	0.073	0.023	0.188		0.110	0.126
Fe^{3+}		0.001				0.015													
Total	2.000	2.000	2.000	2.000	2.000	2.000	2.000	2.000	2.000	2.000	2.000	2.000	2.000	2.000	2.000	2.000	2.017	2.000	2.000
Mg	0.784	0.774	0.759	0.890	0.926	0.977	0.984	0.923	0.937	0.866	0.986	0.740	0.854	0.879	0.481	0.496	0.259	0.695	0.846
Fe^{2+}	0.164	0.136	0.269	0.206	0.107	0.067	0.121	0.169	0.140	0.175	0.109	0.240	0.200	0.138	0.350	0.259	0.459	0.201	0.139
Fe^{3+}	0.085	0.121				0.048				0.011	0.007	0.004		0.021	0.096	0.127	0.186	0.114	0.098
Al	0.005		0.083	0.074	0.029		0.027	0.054	0.039	0.045	0.022	0.027	0.053	0.019	0.034	0.041	0.032	0.037	0.022
Ti	0.047	0.044	0.036	0.017	0.014	0.011	0.011	0.017	0.013	0.023	0.012	0.054	0.023	0.026	0.015	0.057	0.015	0.027	0.027
Mn	0.005	0.007	0.006	0.004	0.003	0.003	0.003	0.003	0.003	0.004	0.003	0.005	0.004	0.003	0.014	0.010	0.027	0.009	0.005
Cr			0.006	0.009	0.039	0.026	0.015	0.011	0.020	0.009	0.014	0.006	0.007	0.009				0.007	0.005
Ni				0.001	0.003		0.002	0.001	0.001		0.002	0.001	0.001	0.001					
Ca	0.868	0.878	0.782	0.761	0.830	0.833	0.802	0.776	0.802	0.821	0.811	0.887	0.826	0.875	0.873	0.916	0.725	0.811	0.804
Na	0.042	0.041	0.058	0.038	0.049	0.035	0.035	0.045	0.044	0.046	0.035	0.035	0.032	0.029	0.137	0.093	0.281	0.100	0.054
Total	2.000	2.000	2.000	2.000	1.999	2.000	2.000	2.000	2.000	2.000	2.000	2.000	2.000	2.000	2.000	2.000	1.983	2.000	2.000
Mg#	83	85	74	81	90	94	89	85	87	83	90	75	81	86	58	66	36	78	86

Table 3: Continued

Sample:	16-05			19-07	16-26			16-05			19-06		16-26		16-05	16-06	19-06	19-07	16-26
Population:	V (mantle)							V (core)							VI				
Analysis:	28	27	25	92	91	46	44	60	61	62	30	32	73	74	3	31	39	104	78
SiO_2	52.24	51.10	52.41	54.39	52.43	53.38	52.20	50.27	52.63	50.04	51.86	52.30	54.08	53.37	51.46	48.94	50.29	49.04	46.44
TiO_2	0.76	1.31	0.91	0.55	1.26	0.53	1.12	1.30	0.74	1.79	1.19	1.30	0.81	0.97	1.34	1.99	1.87	2.59	3.65
Al_2O_3	1.91	2.20	1.24	1.76	2.45	1.58	1.67	2.97	1.46	2.94	2.31	1.65	1.71	1.81	1.72	2.91	3.01	4.40	4.87
Cr_2O_3	1.33	0.57	0.46	1.06	0.62	1.09	0.52	1.24	0.61	0.45	0.98	0.22	0.56	0.36	0.16		0.06		0.05
Fe_2O_3	1.37	2.90	2.18		0.29			3.30	2.16	3.13	0.38	0.79			2.42	4.06	1.48	1.40	3.30
FeO	3.86	3.45	3.62	4.41	5.23	5.23	6.24	3.25	4.40	4.14	4.83	5.79	6.53	7.03	5.10	5.50	6.17	6.85	8.69
MnO	0.09	0.10	0.10	0.09	0.12	0.17	0.12	0.10	0.14	0.12	0.11	0.12	0.17	0.14	0.16	0.16	0.11	0.16	0.18
MgO	16.56	15.71	16.31	17.39	15.57	16.45	14.87	15.73	17.58	14.76	15.43	15.82	15.66	15.11	15.37	13.98	14.07	12.93	11.46
NiO				0.03									0.03						
CaO	21.14	22.46	22.87	21.11	22.51	19.96	22.01	21.12	20.04	22.54	22.24	21.85	20.69	21.24	22.39	21.65	22.03	22.09	20.57
Na_2O	0.56	0.42	0.30	0.65	0.41	0.60	0.37	0.61	0.44	0.43	0.46	0.35	0.47	0.44	0.30	0.43	0.48	0.56	0.68
Total	99.82	100.22	100.40	101.43	100.88	98.99	99.12	99.89	100.21	100.34	99.79	100.19	100.71	100.48	100.42	99.62	99.57	100.02	99.90
Si	1.919	1.882	1.922	1.955	1.914	1.975	1.947	1.857	1.925	1.851	1.914	1.926	1.981	1.965	1.900	1.838	1.877	1.831	1.764
Al	0.081	0.096	0.054	0.045	0.086	0.025	0.053	0.129	0.063	0.128	0.086	0.072	0.019	0.035	0.075	0.129	0.123	0.169	0.218
Fe^{3+}		0.022	0.024					0.014	0.012	0.020		0.002			0.025	0.034			0.018
Total	2.000	2.000	2.000	2.000	2.000	2.000	2.000	2.000	2.000	2.000	2.000	2.000	2.000	2.000	2.000	2.000	2.000	2.000	2.000
Mg	0.907	0.863	0.892	0.932	0.847	0.907	0.827	0.866	0.959	0.814	0.849	0.869	0.855	0.829	0.846	0.783	0.783	0.720	0.649
Fe^{2+}	0.119	0.106	0.111	0.132	0.160	0.162	0.195	0.100	0.135	0.128	0.149	0.178	0.200	0.216	0.158	0.173	0.193	0.214	0.276
Fe^{3+}	0.038	0.058	0.036		0.008			0.078	0.048	0.067	0.011	0.020			0.042	0.081	0.041	0.039	0.076
Al	0.002			0.029	0.020	0.044	0.021				0.014		0.055	0.043			0.009	0.025	
Ti	0.021	0.036	0.025	0.015	0.035	0.015	0.031	0.036	0.020	0.050	0.033	0.036	0.022	0.027	0.037	0.056	0.052	0.073	0.104
Mn	0.003	0.003	0.003	0.003	0.004	0.005	0.004	0.003	0.004	0.004	0.003	0.004	0.005	0.004	0.005	0.005	0.004	0.005	0.006
Cr	0.039	0.017	0.013	0.030	0.018	0.032	0.015	0.036	0.018	0.013	0.029	0.006	0.016	0.011	0.005	0.002	0.002		0.002
Ni				0.001									0.001						
Ca	0.832	0.887	0.899	0.813	0.881	0.792	0.880	0.836	0.785	0.893	0.879	0.862	0.812	0.838	0.886	0.871	0.881	0.884	0.837
Na	0.040	0.030	0.021	0.045	0.029	0.043	0.027	0.044	0.031	0.031	0.033	0.025	0.033	0.031	0.021	0.031	0.035	0.041	0.050
Total	2.000	2.000	2.000	2.000	2.000	2.000	2.000	2.000	2.000	2.000	2.000	2.000	2.000	2.000	2.000	2.000	2.000	2.000	2.000
Mg#	88	89	89	88	84	85	81	90	88	86	85	83	81	79	84	82	80	77	70

Fe_2O_3 and FeO calculated from charge balance (four cations and six O), Mg# = $100Mg/(Mg + Fe^{2+})$. WDS analysis (JEOL 8900 Superprobe).

(Fig. 9). The latter (particularly those <50 μm) can be completely composed of this population. This augite has variable Mg# values (85–69), contains low Cr (commonly below detection limit), and is characterized by high and variable contents of Al (1·7–6·1 wt% Al_2O_3), 1·3–3·6 wt% TiO_2 (Table 3, Figs 10–12) and variable Na (0·3–0·7 wt% Na_2O) with no obvious relationship between Na and Cr (Supplementary Data Fig. S3).

Spinel

Spinel-group minerals, or simply spinel, compose an essential part of the groundmass. They are rarely present as microcrysts and also occur as inclusions in olivine and augite macrocrysts. The crystals are different in morphology, size and internal zonation, and compositional data show the presence of two distinct solid solution series (magnesiochromite–chromite$_{ss}$ and magnetite–ulvöspinel$_{ss}$) (Table 4, Figs 13 and 14).

Euhedral spinel inclusions (up to 180 μm × 90 μm in size) in olivine macrocrysts with normal zonation and microcrysts (up to 160 μm × 110 μm in size) are considered to be the earliest opaque phases to crystallize (Fig. 13a). They are Ti-poor (1·7–3·3 wt% TiO_2) and Al-rich (6·3–8·9 wt% Al_2O_3) magnesiochromite–chromite$_{ss}$. From core to rim contents of Mg and Cr decrease, whereas Al and Ti increase (Fig. 14). Spinel inclusions (up to 30 μm in size) in olivine with reverse zonation are characterized by high and variable Ti (12·1–21·7 wt% TiO_2) and low Cr (3·5–8·5 wt% Cr_2O_3) contents (Fig. 14), although having similar Mg and Al (5·4–7·8 wt% MgO and 7·9–9·6 wt% Al_2O_3) to euhedral chromite (see above).
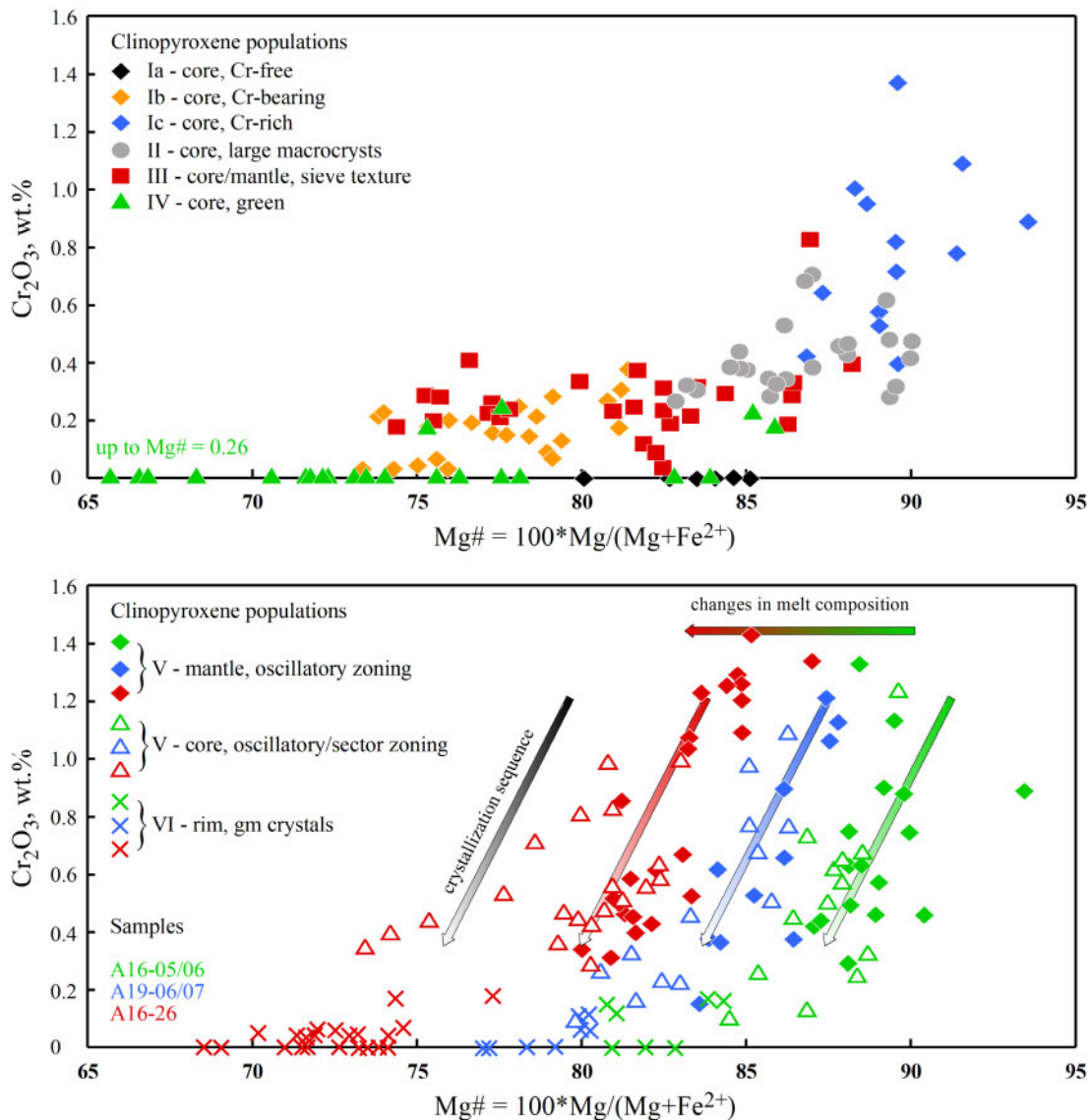

Fig. 10. Relationships between Mg# [$100Mg/(Mg + Fe^{2+})$, calculated from atomic per cent] and Cr_2O_3 (wt%) in clinopyroxene. Arrow 'crystallization sequence' shows compositional changes in population V (core to rim) and from population V to VI. RSD$_{Cr}$ varies between 1 and 7 % dependent on the Cr content.
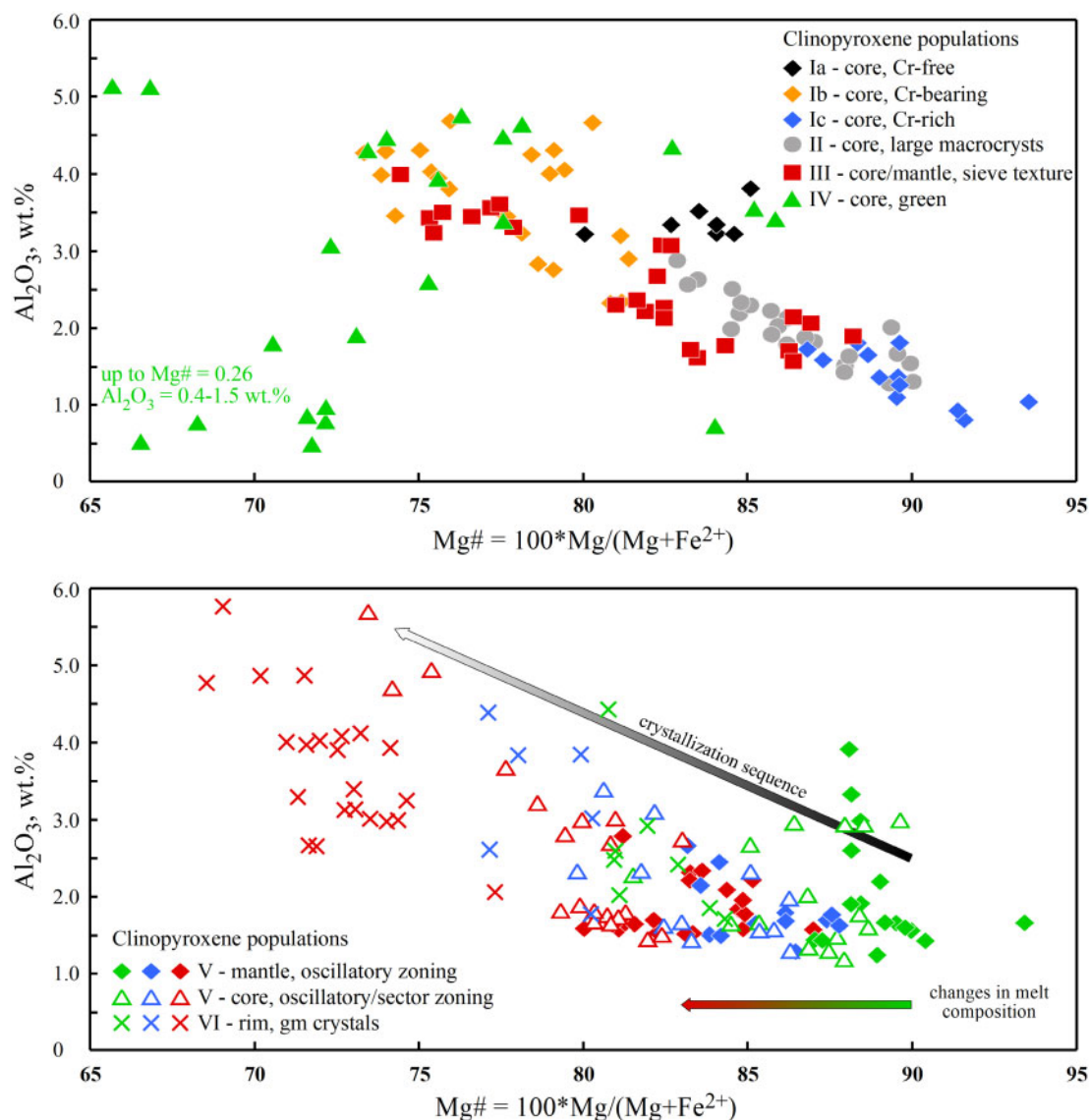
Fig. 11. Relationships between Mg# [100Mg/(Mg + Fe^{2+}), calculated from atomic per cent] and Al$_2$O$_3$ (wt%) in clinopyroxene. Arrow 'crystallization sequence' shows compositional changes in population V (core to rim) and from population V to VI. (For sample numbers see Fig. 10.) RSD$_{Al}$ varies between 1 and 5 % dependent on the Al content.

Strongly zoned euhedral to subhedral spinel-group minerals occur as rare microcrysts (up to 230 μm × 100 μm) and groundmass crystals (Fig. 13b and c). They consist of a chromite core rimmed by 'titanomagnetite' (magnetite–ulvöspinel$_{ss}$). Chromite is a low-Ti variety (2·0–3·8 wt% TiO$_2$) with elevated Al (6·5–10·4 wt% Al$_2$O$_3$) and Mg (3·6–9·6 wt% MgO). The boundary between chromite and magnetite–ulvöspinel$_{ss}$ is gradational with considerable compositional changes over a distance of 5–10 μm (Fig. 14). Magnetite–ulvöspinel$_{ss}$ is Ti-rich (11·2–26·7 wt% TiO$_2$), Cr-poor (1·5–15·7 wt% Cr$_2$O$_3$) and contains less Al (1·1–4·6 wt% Al$_2$O$_3$) and Mg (2·0–4·0 wt% MgO) compared with the core chromite (Fig. 14). One of the studied samples (A19-64) contains texturally and compositionally similar zoned microcrysts with chromite cores and magnetite–ulvöspinel$_{ss}$ rims, but the latter contains ilmenite

exsolution lamellae (Fig. 13d). All magnetite–ulvöspinel$_{ss}$ in this sample, occurring as either rim on chromite or as euhedral to subhedral crystals in groundmass, contains exsolved ilmenite lamellae. Cr-bearing magnetite–ulvöspinel$_{ss}$ (2·2–10·4 wt% Cr$_2$O$_3$, 14·2–19·9 wt% TiO$_2$, Fig. 14) occurs as inclusions in clinopyroxene (typically in varieties II, III, V and VI). Groundmass spinel with grain sizes between 1 and 50 μm (rarely up to 100 μm) occurs as euhedral to subhedral crystals (Fig. 13e). Compositionally it is magnetite–ulvöspinel$_{ss}$ with low Cr (0·2–3·8 wt% Cr$_2$O$_3$), and high Ti (18·2–25·6 wt% TiO$_2$; Fig. 14). A few crystal cores are relatively enriched in Cr (4·1–9·9 and 16·1–17·9 wt% Cr$_2$O$_3$).

All studied samples contain additional anhedral and rather homogeneous spinel (up to 330 μm × 260 μm; Fig. 13f) with Mg, Al and Ti (2·3–4·1 wt% MgO, 1·7–4·0 wt% Al$_2$O$_3$ and 14·5–21·8 wt% TiO$_2$) at levels similar

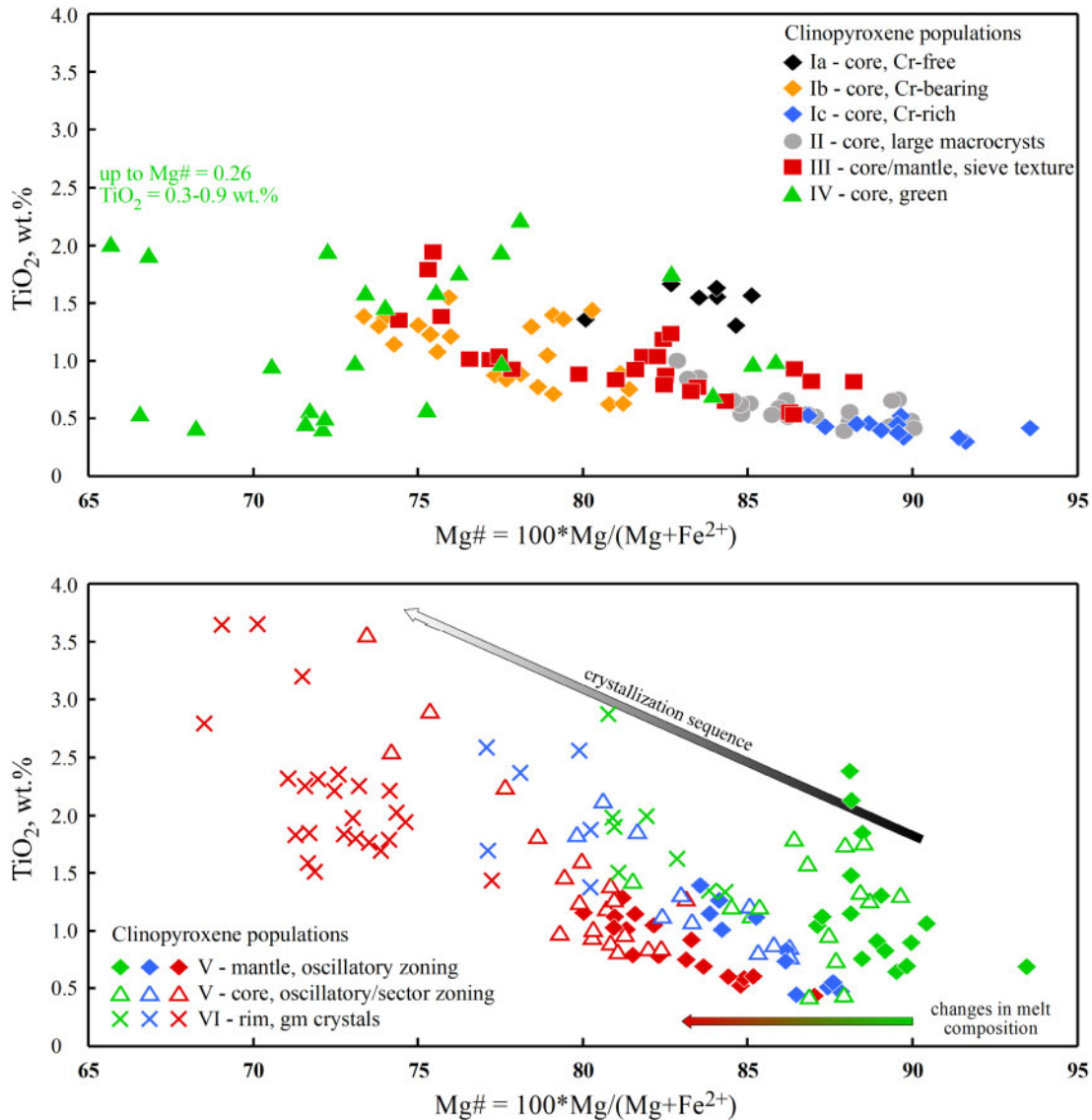**Fig. 12.** Relationships between Mg# [100Mg/(Mg + Fe^{2+}), calculated from atomic per cent] and TiO$_2$ (wt%) in clinopyroxene. Arrow 'crystallization sequence' shows compositional changes in population V (core to rim) and from population V to VI. (For samples numbers see Fig. 10.) RSD$_{Ti}$ varies between 1 and 5 % dependent on the Ti content.

to groundmass magnetite–ulvöspinel (Fig. 15). However, these grains are very low in Cr (mostly below the detection limit; Fig. 14) and compositionally different grains are present within a single specimen; for example, sample A19-08 contains crystals (150–300 μm in size) with very different Ti content (14·5–14·7, 17·0–17·1 and 20·0–20·8 wt% TiO$_2$).

Plagioclase

Plagioclase occurs as subhedral tabular laths to anhedral crystals (mostly 20–70 μm in size, and rarely up to 200 μm in length; Fig. 15a) that form polycrystalline aggregates (Supplementary Data Fig. S4). Plagioclase is andesine–oligoclase solid solution (An$_{0.28–0.37}$Ab$_{0.58–0.66}$Or$_{0.04–0.06}$) with predominance of andesine compositions (Table 5); both minerals contain

minor Sr (0·4–0·6 wt% SrO) and Ba (0·2–0·4 wt% BaO). A single microcryst contains a strongly corroded core with labradorite composition (An$_{0.66}$Ab$_{0.33}$Or$_{0.01}$), rimed by Ca-enriched andesine (An$_{0.42}$Ab$_{0.55}$Or$_{0.03}$). In addition to microcrysts, sample A19-08 contains relatively large embayed plagioclase grains (250 μm × 180 μm to 520 μm × 490 μm; Fig. 15b) of oligoclase composition (An$_{0.20–0.29}$Ab$_{0.67–0.71}$Or$_{0.04–0.09}$).

Apatite

Apatite is a common accessory mineral in all studied samples and occurs as needle- or spindle-like crystals up to 120 μm in length and 10 μm in thickness (Fig. 15c and d; Supplementary Data Fig. S5). Because of the small crystal size WDS analysis was not possible, and SEM–EDS analysis shows that the mineral is close to an

Table 4: Selected analyses of spinel-group minerals

Sample/Variety/Analysis	16-05 (1) core 1	16-05 rim 4	19-06 core 30	19-06 rim 32	19-07 (2) core 62	19-06 (3) core 8	19-06 rim 12	19-04c core 93	19-04c rim 96	19-04c core 39	19-04c rim 40	16-05 (4) core 73	19-06 (5) core 49	19-06 rim 50	19-06 core 44	19-06 rim 46	19-04a core 9	19-08 (6) core 88	19-04a core 23
MgO	12.69	8.51	9.82	9.89	5.44	9.58	3.07	4.81	3.53	5.49	2.07	3.94	2.51	1.69	2.55	1.84	2.28	2.58	3.24
Al_2O_3	7.65	7.17	8.38	8.40	7.89	7.03	4.46	7.45	1.80	8.28	3.44	2.81	6.10	2.69	5.02	3.01	1.23	1.99	3.05
SiO_2	0.09	0.09	0.07	0.08	0.09	0.06	0.05		0.03	0.07	0.08	0.03	0.03	0.10	0.04	0.08	0.04	0.12	0.07
CaO		0.12					0.16	0.05	0.08		0.12	0.08	0.04	0.05	0.06	0.14			
TiO_2	1.77	2.12	3.19	3.19	15.30	2.06	19.41	2.73	18.01	3.47	23.39	14.19	15.14	25.57	18.48	25.00	22.06	17.13	21.17
V_2O_3	0.10	0.09	0.21	0.18	0.57	0.12	0.35	0.12	0.26	0.20	0.33	0.28	0.32	0.35	0.36	0.37	0.32	0.60	0.38
Cr_2O_3	53.91	50.81	44.62	44.04	6.17	51.56	9.61	44.17	3.27	42.48	2.02	10.36	17.88	0.75	9.91	1.06	1.79	0.04	0.08
MnO	0.11	0.19	0.16	0.14	0.32	0.14	0.56	0.50	0.65	0.25	0.63	0.55	0.49	0.70	0.56	0.65	0.74	0.56	0.68
NiO	0.18	0.13	0.15	0.18	0.08	0.14	0.03	0.05	0.09	0.12	0.04	0.09	0.03	0.03			0.07	0.05	0.05
ZnO	0.02	0.10	0.07	0.06	0.07	0.10	0.08	0.24	0.07	0.10	0.09	0.13	0.15	0.09	0.10	0.08	0.10	0.11	0.08
Fe_2O_3	7.95	9.20	12.54	13.11	26.66	8.93	17.90	12.64	30.27	12.12	17.71	29.10	14.82	14.99	17.78	15.88	24.08	34.18	26.45
FeO	14.99	21.55	20.76	20.65	38.30	19.80	44.59	27.38	41.84	27.65	49.20	37.82	41.69	51.49	44.47	50.93	47.49	42.87	45.92
Total	99.47	100.07	99.96	99.90	100.88	99.50	100.28	100.15	99.90	100.21	99.11	99.38	99.18	98.49	99.34	99.03	100.22	100.22	101.16
Fe^{2+}	0.367	0.557	0.499	0.496	0.706	0.506	0.812	0.726	0.782	0.705	0.863	0.761	0.845	0.881	0.842	0.874	0.847	0.837	0.803
Mg	0.625	0.430	0.490	0.494	0.280	0.484	0.164	0.250	0.192	0.282	0.113	0.213	0.135	0.093	0.137	0.101	0.125	0.141	0.173
Mn	0.003	0.005	0.005	0.004	0.009	0.004	0.017	0.015	0.020	0.007	0.019	0.017	0.015	0.022	0.017	0.020	0.023	0.017	0.021
Ni	0.005	0.003	0.004	0.005	0.002	0.002	0.001	0.006	0.003	0.002	0.001	0.003	0.001	0.001	0.000	0.000	0.002	0.002	0.002
Zn	0.001	0.003	0.002	0.001	0.002	0.002	0.002	0.006	0.002	0.002	0.002	0.003	0.004	0.003	0.003	0.002	0.003	0.003	0.002
Total	1.000	0.999	1.000	1.000	1.000	1.000	0.996	0.998	0.998	1.000	0.998	0.998	1.000	1.000	0.999	0.997	1.000	1.000	1.000
Cr	1.408	1.362	1.182	1.167	0.168	1.380	0.272	1.216	0.094	1.159	0.058	0.298	0.509	0.022	0.283	0.031	0.052	0.001	0.002
Fe^{3+}	0.198	0.235	0.316	0.331	0.693	0.228	0.482	0.331	0.831	0.315	0.488	0.796	0.401	0.418	0.484	0.439	0.665	0.942	0.713
Al	0.298	0.286	0.331	0.332	0.321	0.280	0.188	0.306	0.078	0.336	0.149	0.120	0.259	0.117	0.214	0.130	0.053	0.086	0.129
Ti	0.044	0.054	0.080	0.080	0.398	0.052	0.522	0.072	0.494	0.090	0.645	0.388	0.410	0.713	0.503	0.691	0.609	0.472	0.570
Fe^{2+}	0.047	0.054	0.083	0.083	0.401	0.054	0.522	0.072	0.494	0.093	0.645	0.388	0.410	0.715	0.503	0.691	0.610	0.477	0.572
V	0.003	0.002	0.006	0.005	0.016	0.003	0.010	0.003	0.008	0.006	0.010	0.008	0.009	0.010	0.011	0.011	0.010	0.018	0.011
Total	1.997	1.994	1.998	1.998	1.997	1.998	1.996	2.000	1.998	1.998	1.994	1.998	1.998	1.995	1.997	1.994	1.998	1.996	1.997
Si	0.003	0.003	0.002	0.003	0.003	0.002	0.002		0.001	0.002	0.003	0.001	0.001	0.004	0.001	0.003	0.001	0.004	0.002
Ca		0.005					0.006	0.002	0.003		0.005	0.003	0.001	0.002	0.002	0.006			

Varieties: (1) microphenocrysts, inclusions in forsterite (Fo = 84–89 mol%); (2) inclusions in forsterite (Fo = 74–78 mol%); (3) zoned microphenocrysts and inclusions in forsterite (Fo = 84–87 mol%); (4) inclusions in diopside; (5) groundmass crystals; (6) xenocrysts. Fe_2O_3 and FeO calculated from charge balance (three cations and four O). WDS analysis (JEOL 8900 Superprobe).
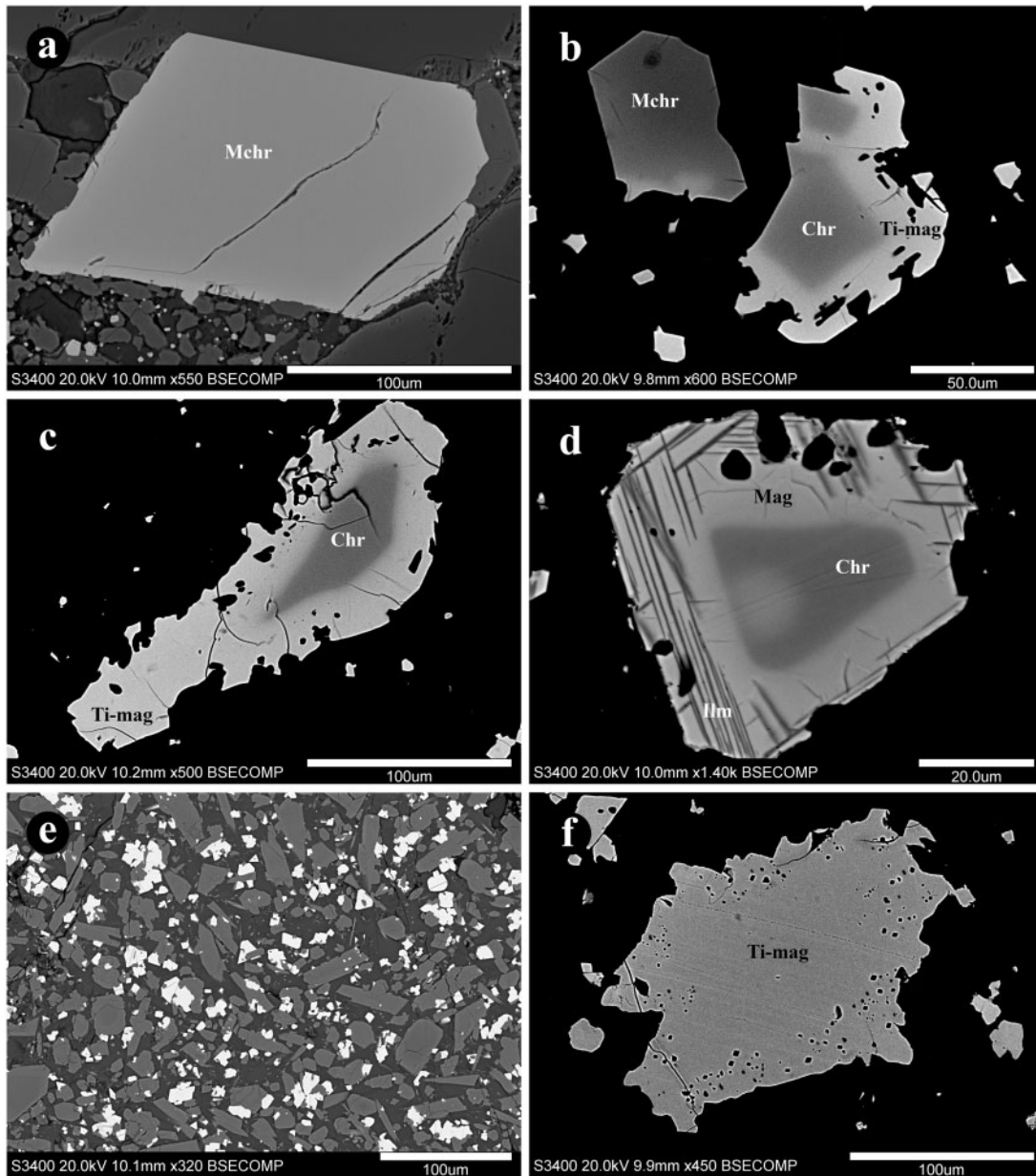
Fig. 13. Morphology and zonation of spinel-group minerals (BSE images). (a) Euhedral magnesiochromite (Mchr) at contact between olivine macrocryst and groundmass, A16-05; (b) euhedral magnesiochromite in olivine macrocryst and zoned chromite (Chr)–magnetite–ulvöspinel$_{ss}$ (Ti-mag) at contact between olivine macrocryst and groundmass, A19-06; (c) zoned chromite (Chr)–magnetite–ulvöspinel (Ti-mag) microcryst, A19-04b; (d) zoned chromite (Chr)–magnetite (Mag) microcryst with ilmenite exsolution (Ilm) in magnetite, A19-64; (e) euhedral to subhedral magnetite–ulvöspinel$_{ss}$ (white) in groundmass, A16-05; (f) anhedral magnetite–ulvöspinel$_{ss}$ microcryst, A19-04a.

ideal fluorapatite with minor Si (*c*. 1·0 wt% SiO_2). No peaks from other cations have been found on ED spectra.

Other minerals

A sample from the Oldoinyo Naisiusiu hill (A19-08) contains rare, but relatively large crystals of perovskite (up to 160 μm × 210 μm in size) (Fig. 15e), a mineral which is not a typical phase in basaltic rocks. It is always surrounded by a 10–50 μm thick rim of ilmenite. The latter, in turn, contains numerous tiny inclusions of REE-rich

mineral(s). Perovskite shows variable Nb contents (0·5–2·1 wt% Nb_2O_5) and is enriched in LREE ($La_2O_3 + Ce_2O_3 + Nd_2O_3 = 2·3–4·1$ wt%, SEM–EDS analysis). Ilmenite is Mg-rich and Nb-bearing with 4·5–4·9 wt% MgO and 0·4–0·7 wt% Nb_2O_5 (SEM–EDS analysis). REE minerals cannot be precisely identified and quantitatively analyzed owing their small size (≤5 μm in size), but SEM–EDS spectra suggest that they represent Ca–REE silicates and rarely REE phosphates.

In addition, the sample contains green clinopyroxene (population IV; Cr-free diopside with 0·9–1·3 wt% Na_2O, 3–6·5 mol% aegirine end-member) with inclusions of
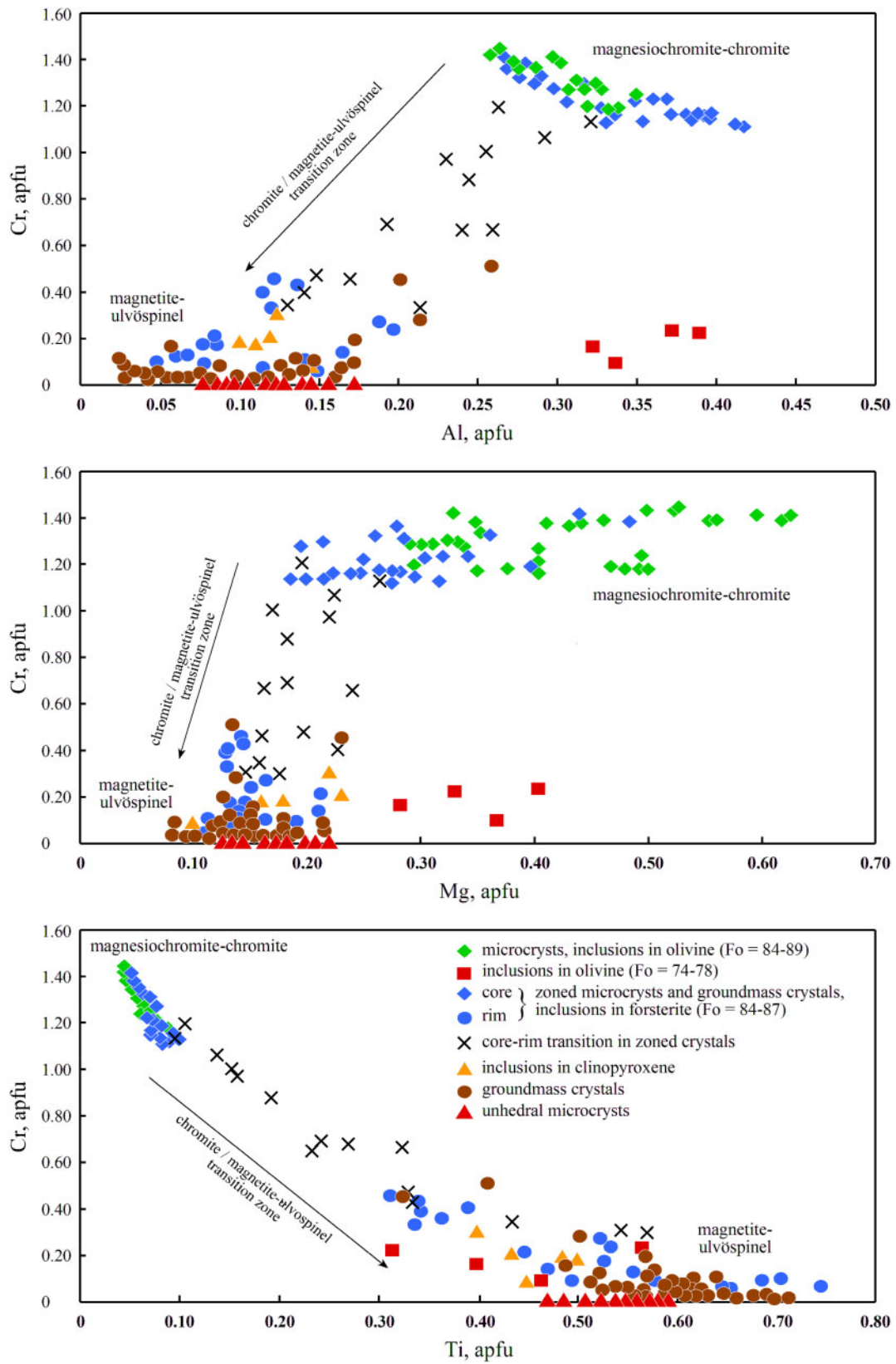
Fig. 14. Compositional variations of spinel-group minerals.

schorlomite (12·6–16·7 wt% TiO_2), titanite (close to an ideal formula) and fluorapatite (Fig. 15f). These were also observed as rare minerals in some of the other samples.

Glass

Glass is an essential component in the studied samples (Supplementary Data Fig. S4). Fresh, unaltered glass is, however, rare (Fig. 15d), but well preserved in two samples from Oldoinyo Emusenge hill (A16-05 and A16-06). The glass contains 58·7–60·2 wt% SiO_2, 18·9–19·4 wt% Al_2O_3 and 13·3–14·6 wt% $Na_2O + K_2O$ (Table 5) and corresponds to a phonolite in a TAS classification diagram (Fig. 4a). It is strongly depleted in Mg (0·5–0·7 wt% MgO) and Ca (0·4–0·9 wt% CaO) and slightly enriched in Fe (4·4–4·7 wt% Fe_2O_{3total}). SEM–EDS analysis shows presence of P (up to 0·5 wt% P_2O_5), Cl (up to 0·4 wt%) and S (up to 0·2 wt% SO_3). The analytical totals are typically between 95 and 98 wt% (Table 5) and this can be an indication of presence of other volatile components (e.g. H_2O). During alteration the glass was transformed to a fine-grained assemblage of montmorillonite, K–Na feldspar, Na ± K zeolite and sodalite (Fig. 15g and h).

Sr–Nd isotopes

Limited published Sr and Nd isotopic compositions for the Ogol basalts are controversial. Whereas the data presented by Mollel (2007) are relatively uniform ($^{87}Sr/^{86}Sr$ = 0·70371–0·70381 and $^{143}Nd/^{144}Nd$ = 0·51255–0·51261), the data from Adelsberger *et al.* (2011) show wide variations ($^{87}Sr/^{86}Sr$ = 0·70350–0·70577 and $^{143}Nd/^{144}Nd$ = 0·51221–0·51257). The highest Sr (0·70577) and lowest Nd isotope (0·51221) ratios were found in sample OL-22E (Adelsberger *et al.*, 2011), which is compositionally different from all other Ogol basalts (picrobasalt with low Si, Mg, Cr and Ni contents and high Ti and P contents; see above) and is probably not directly related to them. In the present study we analysed 10 samples of the Ogol basalts for their Sr and Nd isotopic composition; complemented by three lava samples from the Lemagarut volcano and three samples of basement rocks (Table 6). All measured $^{87}Sr/^{86}Sr$ and $^{143}Nd/^{144}Nd$ ratios were corrected for an age of 2·3 Ma (Mollel, 2007) using the measured $^{87}Rb/^{86}Sr$ ratios.

Our new data (Fig. 16) confirm variable isotopic compositions for the studied basalts ($^{87}Sr/^{86}Sr_{initial}$ = 0·70377–0·70470 and $^{143}Nd/^{144}Nd_{initial}$ = 0·51246–0·51261). The data show a negative correlation between $^{87}Sr/^{86}Sr_{initial}$ and $^{143}Nd/^{144}Nd_{initial}$ ratios, with a sample from Oldoinyo Emusenge hill (A16-05) showing lowest $^{87}Sr/^{86}Sr_{initial}$ and highest $^{143}Nd/^{144}Nd_{initial}$ and a sample from Oldoinyo Mati hill (A19-02) having the highest $^{87}Sr/^{86}Sr_{initial}$ and lowest $^{143}Nd/^{144}Nd_{initial}$ ratios.

Sr–Nd isotopic data for basalts to trachyandesites from the contemporaneously erupting Lemagarut volcano partly overlap with those for the Ogol basalts, forming a continuous field (Table 6; Fig. 16). One sample of Lemagarut trachyandesite (Mollel, 2007), has a
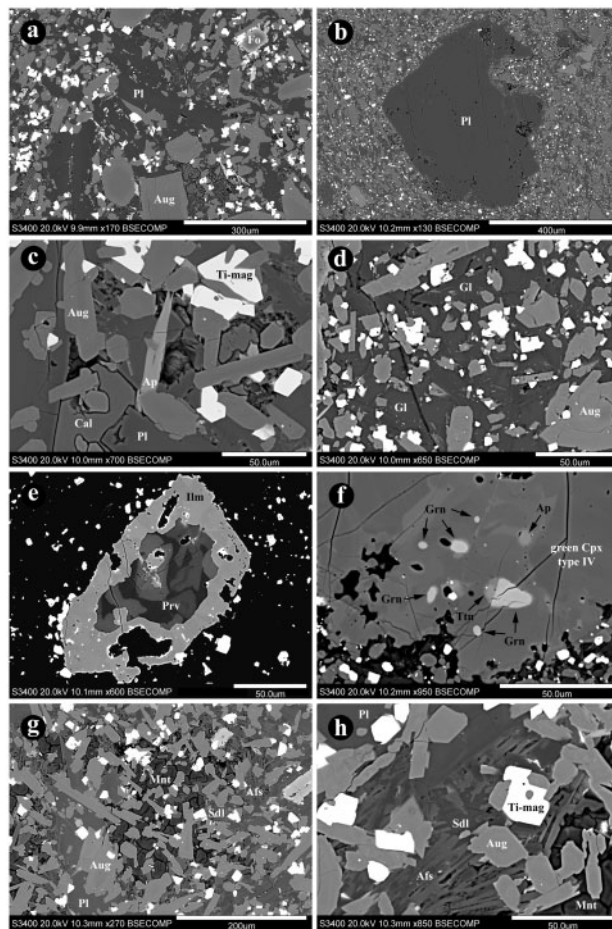

Fig. 15. Macrocrysts, microcrysts and groundmass minerals (BSE images). (a) Andesine (Pl) microcrysts, A19-06; (b) oligoclase (Pl) macrocryst; A19-08, (c) fluorapatite (Ap) in groundmass, A19-07; (d) glass (Gl) with apatite microlites (gray), A16-06; (e) perovskite (Prv) microcryst with ilmenite (Ilm) reaction rim; white inclusions in ilmenite are REE-rich minerals; (f) schorlomite (Grn), titanite (Ttn) and apatite (Ap) in green clinopyroxene (population IV), A19-08; (g, h) glass alteration to montmorillonite (Mnt), K–Na feldspar (Afs), Na zeolite (not shown) and sodalite (Sdl), A16-26; Fo, olivine; Aug, clinopyroxene; Ti-mag, magnetite–ulvöspinel$_{ss}$; Cal, calcite.

low $^{143}Nd/^{144}Nd$ ratio of 0·51219, which is different from all other samples. The reason for the low $^{143}Nd/^{144}Nd$ ratio is unknown, but can potentially be explained by alteration. Significant changes in Nd isotopic compositions were observed for nephelinitic rocks from the nearby Sadiman volcano, where highly altered nephelinitic tuffs have much lower $^{143}Nd/^{144}Nd$ ratios compared with fresh, unaltered tuffs and lavas (Zaitsev *et al.*, 2019).

In contrast to Ogol and Lemagarut, basaltic rocks from the Ngorongoro volcano are characterized by irregular distribution of measured $^{87}Sr/^{86}Sr$ and $^{143}Nd/^{144}Nd$ ratios (Fig. 16). The majority of samples from Ngorongoro show similar to Ogol and Lamagarut ranges for Sr and Nd isotopic compositions ($^{87}Sr/^{86}Sr$ = 0·70405–0·70533 and $^{143}Nd/^{144}Nd$ = 0·51227–0·51277), and three samples have extremely high $^{87}Sr/^{86}Sr$ ratios

Table 5: Selected analyses of plagioclase and glass

Sample:	plagioclase 16-05			16-26			glass 16-05		
Analysis:	2	6	12	1	3	5	1	11	15
SiO_2	60·01	59·90	61·23	59·49	60·69	61·81	57·56	58·96	58·72
TiO_2							0·47	1·11	0·85
Al_2O_3	24·81	24·56	23·53	25·31	24·27	24·00	19·06	18·54	18·76
Fe_2O_3	0·56	0·80	0·77	0·57	0·51	0·57	4·29	4·58	4·30
CaO	7·25	6·87	6·01	7·72	6·53	5·76	0·87	0·44	0·84
MgO	0·04	0·05	0·04	0·06	0·03	0·02	0·71	0·49	0·52
MnO		0·02			0·02	0·02	0·08	0·09	0·07
Na_2O	6·55	6·97	7·47	6·76	7·17	7·52	8·75	7·47	7·55
K_2O	0·74	0·83	0·97	0·70	0·90	1·12	5·52	5·53	5·47
SrO	0·51	0·65	0·45	0·50	0·49	0·45			
BaO	0·19	0·23	0·23	0·27	0·26	0·45	0·03	0·03	0·05
P_2O_5							0·49	0·51	0·40
SO_3									0·16
Cl							0·27	0·28	0·35
$-O=Cl_2$							0·06	0·06	0·08
Total	100·66	100·87	100·71	101·38	100·87	101·71	98·03	97·96	97·96
Si	2·674	2·672	2·727	2·642	2·700	2·727			
Al	1·303	1·291	1·235	1·325	1·273	1·248			
Fe^{3+}	0·019	0·027	0·026	0·019	0·017	0·019			
Total	3·996	3·990	3·988	3·986	3·989	3·993			
Ca	0·346	0·328	0·287	0·367	0·311	0·272			
Na	0·566	0·603	0·645	0·582	0·618	0·643			
K	0·042	0·047	0·055	0·040	0·051	0·063			
Mn	0·000	0·001	0·000	0·000	0·001	0·001			
Mg	0·003	0·003	0·003	0·004	0·002	0·002			
Sr	0·013	0·017	0·012	0·013	0·013	0·011			
Ba	0·003	0·004	0·004	0·005	0·005	0·008			
Total	0·973	1·003	1·006	1·011	1·001	1·000			

P, S and Cl were not analysed in plagioclase. WDS (plagioclase, JEOL 8900 Superprobe) and EDS (glass, Hitachi S-3400N) analyses.

of 0·70634, 0·70801 and 0·71317 (Nonnotte, 2007; Mollel et al., 2008).

Importantly, the Sr and Nd isotopic data for the Ogol basalts, as well as the basaltic rocks from Lamagarut and Ngorongoro, correlate with their major element whole-rock data (Fig. 17). The $^{87}Sr/^{86}Sr$ ratios correlate positively with SiO_2, Al_2O_3, Na_2O and K_2O, and negatively with MgO, TiO_2, Fe_2O_3 and CaO, whereas $^{143}Nd/^{144}Nd$ ratios show the opposite relationship.

DISCUSSION

Primary and xenocrystic minerals

The textural and compositional differences between the various populations of olivine, clinopyroxene, spinel group minerals and plagioclase in the studied samples (see above) suggest that macrocrysts, microcrysts and groundmass minerals represent primary minerals (autocrysts and microlites), which crystallized from a particular melt batch erupted as lava, but also comprise variable amounts of xenocrysts.

As primary minerals we consider the following:

1. olivine macrocrysts with normal zonation and generally unzoned microcrysts (Fig. 7a and b);
2. clinopyroxene cores and mantles with characteristic oscillatory-type, rarely sector-type or continuous growth zonation (population V) and augite rims (population VI; Fig. 9);
3. magnesiochromite–chromite as inclusions in olivine with normal zonation and microcrysts, magnetite–ulvöspinel$_{ss}$ rims around those and discrete magnetite–ulvöspinel$_{ss}$ crystals in groundmass (Fig. 13a–e);
4. (4) microcrysts and groundmass andesine–oligoclase$_{ss}$ and fluorapatite (Fig. 15a and c).

Crystals of all other minerals populations are considered to represent xenocrystic material of different origin, although some of them can represent antecrysts:

1. olivine crystals (and subhedral to anhedral fragments thereof) that show reverse and repetitive zonations (Fig. 7c–f) and their Cr-bearing magnetite–ulvöspinel$_{ss}$ inclusions;
2. rounded and embayed clinopyroxene cores (populations I–IV) and subhedral fragments thereof (Fig. 9a–g), including perovskite, rimmed by ilmenite and scholromite ± apatite and titanite (Figs 9f and 15e, f) that occur as inclusions in population IV (green cores);
3. anhedral, low-Cr magnetite–ulvöspinel$_{ss}$ (Fig. 13f) and embayed oligoclase macro- and microcrysts (Fig. 15b).

The presence of abundant and texturally or compositionally diverse xenocrystic minerals suggest an open-system

Table 6: Rb–Sr and Sm–Nd data for samples of the Ogol and Lemagarut lavas and the Precambrian rocks

Sample	Rb (ppm)	Sr (ppm)	$^{87}Rb/^{86}Sr_m$	$^{87}Sr/^{86}Sr_m$	$^{87}Sr/^{86}Sr_i$	Sm (ppm)	Nd (ppm)	$^{147}Sm/^{144}Nd_m$	$^{143}Nd/^{144}Nd_m$	$^{143}Nd/^{144}Nd_i$	εNd
Ogol lavas											
A16-05	20.9	562	0.1077	0.703771 ± 9	0.703768	8.17	40.8	0.1211	0.512616 ± 6	0.512614	−0.41
A16-06	17.1	735	0.0670	0.703903 ± 15	0.703901	9.79	51.2	0.1158	0.512579 ± 3	0.512577	−1.13
A16-25	24.2	786	0.0890	0.703907 ± 17	0.703904	9.69	52.5	0.1117	0.512553 ± 4	0.512551	−1.63
A16-26	23.3	845	0.0796	0.704088 ± 10	0.704085	9.28	49.8	0.1126	0.512561 ± 3	0.512559	−1.48
A19-02	23.9	991	0.0696	0.704704 ± 11	0.704702	8.59	43.6	0.1191	0.512462 ± 4	0.512460	−3.41
A19-4c	28.2	851	0.0958	0.704367 ± 10	0.704364	9.98	54.6	0.1106	0.512511 ± 5	0.512509	−2.45
A19-06	24.3	752	0.0931	0.704180 ± 16	0.704177	9.39	48.7	0.1166	0.512572 ± 3	0.512570	−1.26
A19-07	27.0	823	0.0948	0.704075 ± 9	0.704072	9.46	50.9	0.1124	0.512546 ± 3	0.512544	−1.77
A19-08	15.2	784	0.0561	0.704325 ± 9	0.704323	9.10	49.5	0.1111	0.512493 ± 5	0.512491	−2.80
A19-64	19.4	881	0.0635	0.704359 ± 9	0.704357	8.33	43.7	0.1152	0.512541 ± 5	0.512539	−1.87
Lemagarut lavas											
A16-21	56.2	1043	0.1557	0.705000 ± 10	0.704995	14.4	84.7	0.1029	0.512422 ± 3	0.512420	−4.19
A16-28	69.6	1086	0.1852	0.704949 ± 13	0.704943	13.1	76.0	0.1039	0.512421 ± 3	0.512419	−4.21
A16-29	46.1	1397	0.0953	0.704980 ± 19	0.704977	11.7	63.3	0.1117	0.512414 ± 2	0.512412	−4.34
Precambrian basement											
A16-10	4.08	124	0.0950	0.704687 ± 11	0.704684	4.00	13.9	0.1741	0.512378 ± 5	0.512375	−5.07
A16-12	222	146	4.4560	0.862926 ± 14	0.862783	3.80	21.8	0.1053	0.511058 ± 5	0.511056	−30.79
A16-16c	17.0	336	0.1465	0.709289 ± 14	0.709284	3.27	15.5	0.1276	0.511452 ± 6	0.511450	−23.12

A16-10, green schist; A16-12, granite–gneiss; A16-16c, garnet amphibolite. m, measured; i, initial (calculated for 2.3 Ma). $^{143}Nd/^{144}Nd$ radio is normalized to $^{146}Nd/^{144}Nd = 0.7219$, error is 2 standard error of the mean in the last digits.
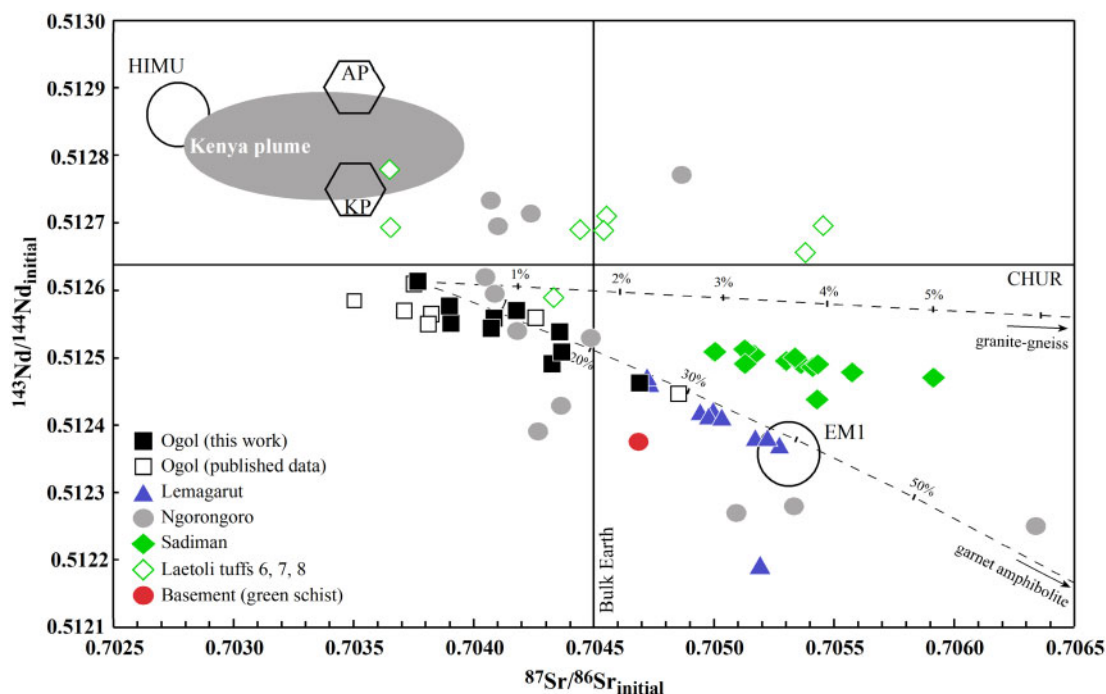
Fig. 16. Sr and Nd initial ratios (2·3 Ma) for the Ogol basalts, Lemagarut, Ngorongoro and Sadiman volcanoes, Laetoli tuffs and green schist from the Tanzania Craton. Data are from this study and Paslick *et al.* (1995, 1996), Mollel (2007), Nonnotte (2007), Adelsberger *et al.* (2011) and Zaitsev *et al.* (2012, 2019). Dashed lines show mixing isotope models between Ogol basalt (A16-05), granite–gneiss (A16-12) and garnet amphibolite (A16-16c). Mantle end-members (HIMU and EM1) are from Hart *et al.* (1992) and Bell & Tilton (2001). Kenya plume is from Aulbach *et al.* (2011), AP, Afar plume (Rogers *et al.*, 2000); KP, Kenya plume (Rogers *et al.*, 2000). The 2σ values of the measured $^{87}Sr/^{86}Sr$ and $^{143}Nd/^{144}Nd$ values are 0·000009–0·000019 and 0·000002–0·000006 respectively (Table 6).

and multi-stage crystallization history for the Ogol basalts, providing evidence for several stages of mixing and mingling during their evolution, and these are considered in the following.

Origin of xenocrystic minerals

Importantly, primary olivine with normal zonation and xenocrystic olivine with reverse zonation occur in the same sample, and rim compositions for both populations are very similar (Fig. 8). This indicates that xenocrystic olivine cores (in reversely zoned crystals) were entrained in the magma before eruption with a residence time long enough for partial equilibration and overgrowth. An olivine megacryst with Fe-rich core and normal zonation (see above) was also probably entrained before eruption, because the crystal rim has a different composition from rims on normally zoned Fe-poor olivine in the same sample. Olivine with repetitive zonation (Fe-rich core–Fe-depleted mantle–Fe-rich rim; Fig. 7e and f), although being extremely rare, is an example of multi-stage growth in melt (or melts) with variable Mg#. Unzoned subhedral fragments, with or without kink-banded texture, point to entrainment close to the surface, only shortly before lava eruption and with no time for equilibration with the surrounding melt and rim overgrow.

All studied olivine crystals, including kink-banded crystals, show higher contents of Ca and Mn (0·17–0·42 wt% CaO and 0·12–0·38 wt% MnO) compared with mantle olivine (Fo$_{\geq 90}$), which has typically up to 0·1 wt% and rarely up to 0·2 wt% oxides (e.g. Simkin & Smith, 1970; Dawson, 2002; Koornneef *et al.*, 2009). Therefore, we assume that the Ogol lavas contain basaltic olivine only and none of the xenocrysts derive from mantle lithologies. Rare kink-banded crystals can derive from deformed cumulate ultramafic to mafic rocks formed at crustal level, or they may be kinked during emplacement of the basaltic magma (e.g. Li *et al.*, 2012; Bradshaw *et al.*, 2018).

Two possible scenarios can explain the occurrence of both low- and high-Fe olivine: (1) mixing of relatively primitive magma with evolved magma batches related to the differentiation of the primary Ogol magmas; (2) mixing with evolved melts derived from the Lemagarut volcanic system, which was active at the same time as the Ogol magmas erupted. The second scenario is supported by the occurrence of embayed oligoclase crystals in the Ogol basalts (Fig. 15b), as their morphology and composition suggest that they represent xenocrysts. Lavas of basaltic trachyandesite with plagioclase as phenocrysts have been observed in the Laetoli area (samples A16-21 and A16-28, Supplementary Data Table S1) and on the western lower slope of the Lemagarut volcano; our unpublished data show that these plagioclase phenocrysts are compositionally similar to embayed oligoclase crystals found in the Ogol basalts.
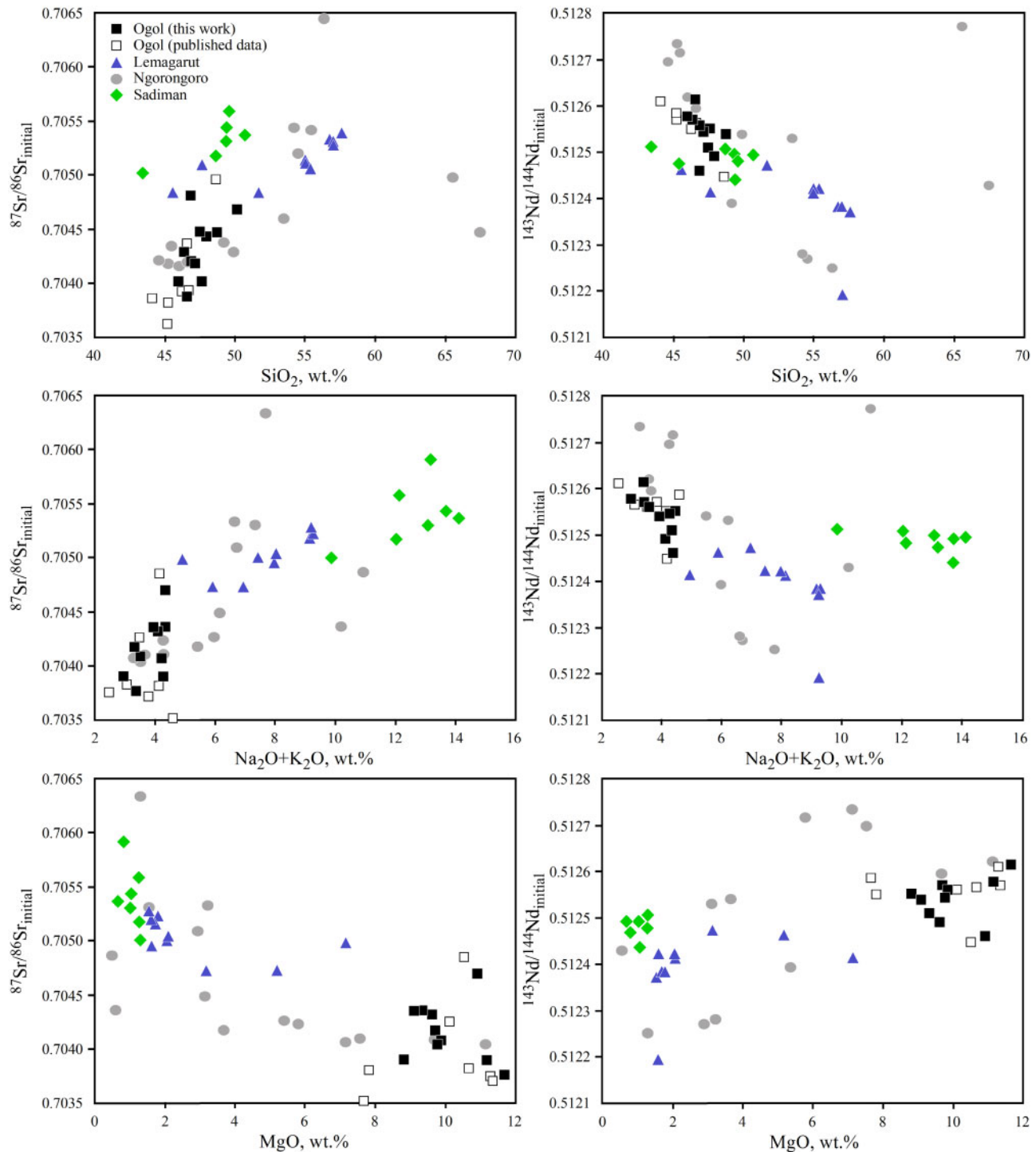
Fig. 17. Relationships between Sr and Nd initial isotope ratios and major elements for the Ogol basalts and Lemagarut, Ngorongoro and Sadiman volcanoes. Data are from this study and Mollel (2007), Nonnotte (2007), Adelsberger *et al*. (2011) and Zaitsev *et al*. (2012).

Green core clinopyroxenes (population IV) with inclusions of schorlomite, titanite and apatite (Figs 9f and 15f), as well as discrete perovskite crystals (Fig. 15e) provide strong evidence for the additional contribution of evolved nephelinite- or foidolite-type contaminants—either by mixing between the basaltic Ogol melts and mantle-derived nephelinitic melts or by

assimilation or fragmentation of already crystallized foidolitic rocks at depth.

However, no nephelinitic rocks with an age of *c*. 2·3 Ma are known in the Crater Highlands and adjacent Olduvai Gorge areas, and here alkaline nephelinite to phonolite magmatism (Sadiman volcano, Laetolil tuffs, Engelosin cone, Mollel, 2007; Zaitsev *et al*., 2012, 2019)

is older (>3 Ma). We can only speculate that nephelinite-type magmas were still present at depth after 3·0 Ma and mixed with Ogol melts at mantle or crustal levels. This assumption is somewhat supported by alkaline volcanoes in the Gregory Rift, which were active at 2·3 Ma; for example, Tarosero volcano (Mana *et al.*, 2015; Braunger *et al.*, 2021). At Crater Highlands alkaline magmatism was reactivated around 1·2 Ma (Fig. 1) with the Embagai volcano being active at 1·2–0·8 Ma (Fig. 2).

Alternatively, the minerals can simply derive from small-scale assimilation of unexposed cumulitic meltei-gite–ijolite (foidolitic) rocks and/or nephelinites related to the Sadiman volcano (Zaitsev *et al.*, 2012) or even from the Laetolil melilite nephelinite tuffs (Zaitsev *et al.*, 2019) by ascending basaltic melts. Perovskite and schorlomite are relatively common minerals in Sadiman and in the Laetolil tuffs. However, these rocks contain perovskite as euhedral crystals (this suggests equilibrium with the host melt) or as relics in titanite (high silica activity; see fig. 7b of Zaitsev *et al.*, 2012) and an ilmenite replacement rim was never observed. Perovskite + ilmenite assemblages are known from kimberlites, but the minerals show opposite relationships, with primary ilmenite and a perovskite reaction rim around it (e.g. Mitchell, 1972). Formation of ilmenite on perovskite could be an indication of relatively high iron and low silica activity compared with conditions needed for titanite formation. Perovskite is also known from alkaline rocks at the extinct nephelinitic Mosonik and Kerimasi volcanoes (Church, 1995; Paslick *et al.*, 1996) and from recent olivine melilitites and nephelin-ites at Oldoinyo Lengai (Keller *et al.*, 2006; Dawson, 2008).

One of the studied green core crystals (Fig. 9g) is different from the others as it shows a distinct patchy zonation. It contains 0·17–0·24 wt% Cr_2O_3, and is mantled by augite population V. It should be noted that all other green cores are rimmed by augite VI only and some crystals even do not have the rim. This suggests that entrainment of this crystal happened at a different depth level and time, but the detailed origin of this crystal remains unclear. Augite population Ia (Fig. 9a) could be also related to a nephelinite-type contaminant because of the lack of Cr. It is always mantled by augite V; these crystals had a long residence time in the melt and therefore another, probably deeper, mixing event compared with clinopyroxene IV, is considered.

Rounded and embayed clinopyroxene cores (populations Ib and Ic) are mantled by primary augite V followed by a rim of augite VI, whereas clinopyroxene II cores are rimmed by augite VI but lack a mantle of augite V. This may suggest different residence times in melt(s). Compositionally, they are also different, but plotting all together they show gradational changes. From augite Ic, via augite II, to augite Ib we observe decreasing Mg# (94–73) and Cr_2O_3 (from 1·4 to to 0·05 wt%), accompanied by increasing Al_2O_3 (from 0·8 to 4·7 wt%) and TiO_2 (from 0·3 to 1·6 wt%) content (Figs

10–12). These variations suggest crystallization of minerals from melts with different compositions. All cores of augite Ib and Ic, and even megacrystic augite II, are relatively homogeneous (Fig. 9) with small compositional variations within a single crystal. We suggest that they crystallized in closed-system intermediate magma chambers under equilibrium conditions. The compositional variations in augite Ib, Ic and II are similar with those of primary augite V (Figs 10–12). This indicates basaltic melt compositions that may derive from the Lemagarut magmatic system and were mixed with Ogol melts.

Alternatively, high-Mg# and high-Cr augite Ic may derive from mantle rocks. Although mantle xenoliths are not known from basaltic or nephelinitic rocks of the Crater Highlands, they occur, for example, at Lashaine volcano within the Gregory Rift, at Labait volcano located on the eastern edge of the Tanzanian Craton and other localities. Clinopyroxene from Lashaine (Dawson, 2002) is enriched in Cr and Na (1·7–3·1 wt% Cr_2O_3 and 1·2–2·5 wt% Na_2O) compared with that from Ogol, but clinopyroxene occurring in glassy melt pockets, veinlets and veins shows similar levels of Cr and Na (0·2–1·8 wt% Cr_2O_3 and 0·3–0·8 wt% Na_2O) to augite Ic. However, as no 'true' mantle minerals (e.g. low-Ca–Mn and high-Fo olivine, high-Cr–Na clinopyroxene and/or orthopyroxene) were found in the Ogol basalts we suggest that a basaltic contaminant component is more likely for augite Ic.

Spongy clinopyroxene cores and mantles (population III) are compositionally similar to augite populations Ib and II and even partly overlap with augite Ic (Fig. 9d and e) and are always overgrown by augite V, indicating relatively long residence time in the melts. The large compositional variations for augite III (Figs 10–12) are interpreted to represent magmatic differentiation. Spongy- or sieve-textured minerals, mainly plagioclase and pyroxene, are known in various volcanic rocks and two models were suggested to explain the origin of the texture (e.g. Nelson & Montana, 1992; Stewart & Pearce, 2004; Shane *et al.*, 2019). The formation of spongy-textured crystals can be related to magma mixing processes or may be due to rapid decompression during melt ascent.

Characteristics of primary minerals

Primary orthomagmatic macrocrysts of olivine and clinopyroxene (population V) are Mg-rich ($Fo_{89.5}$ and Mg# of 94, respectively) and crystallized from rather primitive melts with Mg# of 72·5–70·5 [assuming crystal/melt equilibrium with $Kd_{Fe/Mg}$(ol/liq) = 0·30–0·35, depending on pressure; Ulmer, 1989]. Primary olivine with lower Mg contents (down to $Fo_{84.2}$) reflect magmatic differentiation or magma mixing processes, or combinations thereof.

Similarly, the compositional variation of augite V is explained, characterized by well-developed zonation with a decrease of Mg# and Cr from core to rim (in the case of

mantle from inner to outer parts) and a simultaneous increase in Al and Ti (Figs 11 and 12). Augite VI that occurs as rims around macro- and microcrysts and as groundmass crystals, formed somewhat later but from the same evolving magma. Based on its textural context and evolved composition (low Mg# and high content of Al and Ti), we suggest that augite VI crystallized immediately before and during eruptions of melts.

Two compositionally distinct spinel group minerals crystallized during magmatic differentiation. The change from magnesiochromite–chromite$_{ss}$ to magnetite–ulvöspinel$_{ss}$ not only indicates changes in melt composition, but also is related to changes in physical-chemical conditions, such as temperature and oxygen fugacity (Hill & Roeder, 1974).

Ogol primary melt composition

The relatively high concentrations of Cr and Ni in the studied samples allow them to be considered as candidates for primary magma compositions, not only for the Ogol rocks, but also for the Lemagarut and even Ngorongoro volcanoes (see above). The Ogol basalts are relatively primitive (Table 1), but show continuous variations in contents of major and trace elements (Fig. 4). With 11·5 wt% MgO (Mg# = 61), 975 pm Cr and 222 ppm Ni, a sample from Oldoinyo Emusenge hill (A16-05; Fig. 6a) could approximate the composition of a primary magma in equilibrium with its mantle source. Out of all studied samples, A16-05 contains the most Mg-rich olivine (Fo$_{89·5–87·5}$) and clinopyroxene V (Mg# of 94–85) and magnesiochromite. Also, it is characterized by the lowest $^{87}Sr/^{86}Sr_i$ (0·703768) and highest $^{143}Nd/^{144}Nd_i$ (0·512614) ratios compared with the Ogol as well as Lemagarut basalts. However, even this sample contains a few high-Fe olivines as well as xenocrystic augite (populations Ib, Ic, II and IV). Therefore, we suggest that its composition is close to but does not exactly correspond to a primary melt composition. The presence of relatively Fe-rich and Ni-poor olivine causes a decrease of Mg and Ni and an increase of Fe compared with an initial composition (Supplementary Data Fig. S6). Likewise, abundant augite xenocrysts mainly influence Mg, Fe and Cr content of the whole-rock. The lack of trace element data for primary and xenocrystic minerals does not allow a more detailed discussion on possible changes, particularly for trace elements, of initial composition of melts.

Despite the modification of the studied samples by variable amounts of xenocrystic minerals (see above), their minor and trace element distribution is similar to that of ocean island basalt (OIB) (Fig. 5), except for Ba and Cs. The relative depletion of the Ogol basalts in K could reflect partial melting in the presence of a K-bearing phase (amphibole and/or phlogopite) as suggested for other volcanic rocks in the NTD zone (e.g. Mana et al., 2015). Both minerals are known in mantle xenoliths from Eledoi and Pello Hill, where they form metasomatic veins (Dawson & Smith, 1988), and giant mantle-derived amphibole and mica megacrysts (up to 12 cm in size) occur at Deeti cone (Johnson et al., 1997; Zaitsev et al., 2013). The high values of [(Tb/Yb)$_{CN}$ = 2·48–2·83] observed in the Ogol basalts indicate melting of enriched lithosphere in the presence of residual garnet (Wang et al., 2002), as previously suggested for Ngorongoro basaltic rocks (Mollel et al., 2008) and Turkana lavas (Furman et al., 2006). Such a mantle source for the basalts is also supported by relatively high Ce/Pb ratios of 17·3–24·9.

Crystallization depth and temperature of the Ogol basalts

Based on the clinopyroxene-only barometer of Nimis & Ulmer (1998), there is no clear evidence for a deep (mantle) origin of the various xenocrysts (populations I–IV). Also, pressure estimates for xenocrysts and orthomagmatic clinopyroxene (populations V and VI) are rather similar, although with many of them illustrating negative, and thus, geologically meaningless crystallization depths (Supplementary Data Fig. S7). Apparently, such pressure estimates are not suitable in this case. It is known that melt composition influences clinopyroxene composition as well. Therefore, we used augite populations V and VI to constrain the crystallization pressure and temperature by applying the clinopyroxene–liquid barometer of Neave & Putirka (2017) combined with the thermometer equation (33) of Putirka (2008).

As a proxy for the liquid composition in equilibrium with augite, we used whole-rock compositions, being aware that (1) the whole-rock composition cannot represent the coexisting liquid for both augite populations V and VI, as these crystallized over certain intervals and partly during different stages, and that (2) mineral removal as well as accumulation or xenocryst entrainment result in discrepancies between equilibrium melts and the whole-rock compositions. Correction of the whole-rock composition by removing xenocrysts was rejected because the amount of xenocrysts cannot be determined exactly. We still applied the thermobarometer, as the required liquid components of the pressure equation solely involve the Al, Na, K and Si concentration (Neave & Putirka, 2017). The aluminum and alkali element budget of the whole-rock compositions is mainly controlled by plagioclase, and the relatively high SiO$_2$ concentration of the basalts ($\sim$45 wt%) acts as a buffer, hence diminishing the effect of olivine, clinopyroxene or spinel contamination. It should be noted that the temperature equation (33) of Putirka (2008) depends on further liquid components (Ca, Mg, Fe, Ti concentration), on which xenocryst contamination, however, has little effect (Supplementary Data Fig. S8). To obtain reliable results, two important criteria for the pressure calculations have to be satisfied (e.g. Putirka et al., 1996; Putirka, 2008; Neave & Putirka, 2017). First, the Fe and Mg concentrations of clinopyroxene and the coexisting liquid must be in accordance with the assumed Fe–Mg

exchange coefficient of $K_D[Fe–Mg]^{cpx–liq} = 0.27 \pm 0.3$ (Fig. 18a). Equally important is that the observed augite composition conforms with the predicted values (Fig. 18b), for which we used $\pm 5\%$ as the range cutoff. If these requirements are not fulfilled, clearly meaningless pressure variations down to –25 kbar are calculated (Fig. 18c). Data that meet these requirements (Fig. 18c), however, suggest formation pressures for augite V typically between 1 and 4 kbar (uncertainty of ± 1.4 kbar) at a temperature of $\sim$1150–1220 °C (uncertainty of ± 45 °C). The calculated pressures indicate upper-crustal crystallization depths for augite V of c. 3–12 km, which is consistent with several basaltic magmas at other localities (e.g. Eimeishan; Icelandic rift zone; Tao *et al.*, 2015; Neave & Putirka, 2017). Groundmass augite VI does not meet the equilibrium constraints, which is related to the relatively evolved composition of late-stage augite VI compared with early magmatic augite V (Fig. 18a). The groundmass assemblage of augite VI, olivine and magnetite–ulvöspinel$_{ss}$, however, would be suitable for calculating equilibrium temperature, silica activity and oxygen fugacity using the QUIIF software package (Andersen *et al.*, 1993). Whereas late-stage augite and magnetite–ulvöspinel$_{ss}$ are in textural equilibrium, there is, however, no clear evidence that olivine crystallized contemporaneously. Indeed, the high uncertainty ($>$100 °C) of the calculated temperature and oxygen fugacity (above 3 log units), as well as the failure to calculate the silica activity (iteration limit) clearly points towards chemical disequilibrium between olivine on the one hand, and augite VI + magnetite–ulvöspinel$_{ss}$ on the other hand (Supplementary Data Table S3). Hence, we consider the calculated results as not reliable.

Evidence for magma hybridization in the Ogol basalts

The variability of the Ogol basalts in mineralogy, whole-rock compositions, incompatible trace element ratios (e.g. Ce/Pb, La/Sm) and Sr–Nd isotopic ratios reflects the contribution of different components, two of which (basaltic and nephelinitic) are suggested above. Furthermore, assimilation of crustal rocks composing the Tanzanian Craton may contribute as considered for other volcanic rocks in the Gregory Rift and Crater Highlands (e.g. Mollel *et al.*, 2008; Mana *et al.*, 2015).

Archean basement exposed in the southwestern part of the NTD zone close to Laetoli, allows us to consider granite–gneisses and associated garnet amphibolites (Supplementary Data Table S1) as possible contaminants. Garnet amphibolite is unlikely to explain the observed $^{87}Sr/^{86}Sr$ and $^{143}Nd/^{144}Nd$ variations, as up to 25% assimilation would be needed to cover this range and such a voluminous addition would be reflected in the whole-rock composition of the Ogol basalts (Fig. 16). Assimilation of granite–gneisses would require only $<$3% bulk assimilation but the mixing line between Ogol basalts and granite–gneiss is shifted to higher
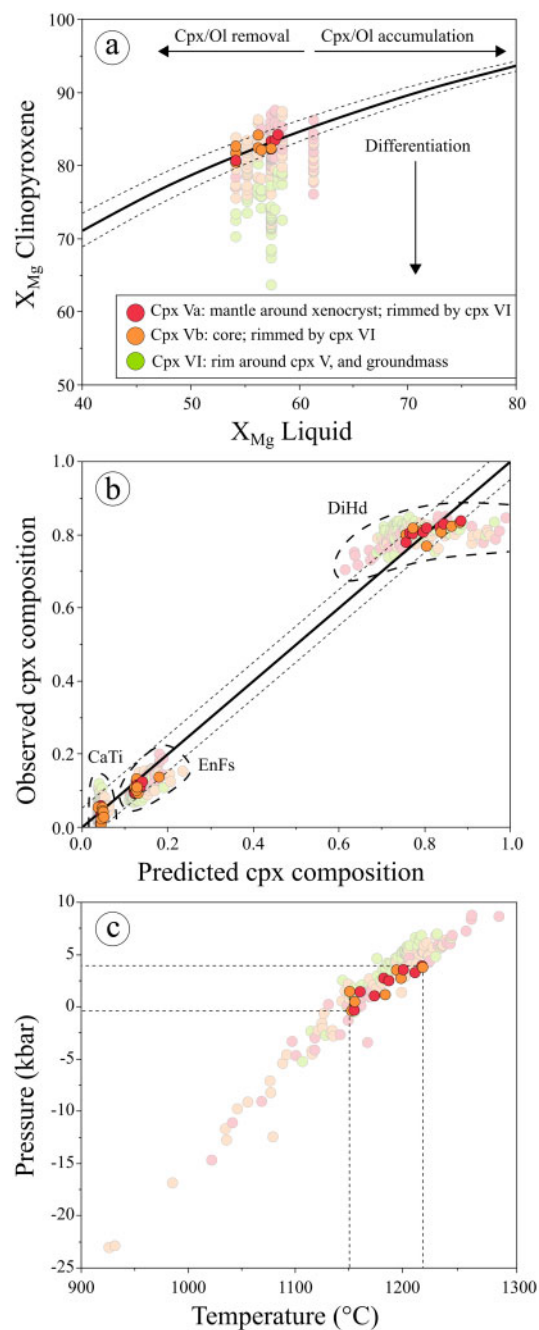

Fig. 18. Clinopyroxene–liquid thermobarometry for the Ogol basalts according to Neave & Putirka (2017), paired with the temperature equation (33) of Putirka (2008). The whole-rock composition was used as a proxy for the liquid coexisting with clinopyroxene. (a) Rhodes diagram (X_{Mg} clinopyroxene vs X_{Mg} liquid) for the studied basalts. X_{Mg} is $100Mg/(Mg + Fe_{tot})$, molar. The curves illustrate the equilibrium interval between clinopyroxene and liquid by assuming an exchange coefficient $K_{D(Fe–Mg)}^{cpx–liq}$ of 0.27 ± 0.3. (b) Observed clinopyroxene compositions vs predicted clinopyroxene compositions including diopside–hedenbergite (DiHd), enstatite–ferrosilite (EnFs) and Ti-Tschermak's clinopyroxene (CaTi; Putirka, 2008). The accepted range of equilibrium is indicated by the dashed lines ($\pm 5\%$, absolute). The predicted DiHd component sometimes exceeds 1.0 (up to 2.3), with the corresponding pressure calculations giving extraordinary low values less than –5 kbar. (c) Pressure–temperature correlation of the applied thermobarometer. The results that fulfil the equilibrium constraints are highlighted.

^{143}Nd/^{144}Nd values. An alternative explanation for the observed variations is the addition of a nephelinite-type component, for which data from the Sadiman volcano were used (sample Sad-10; Zaitsev *et al.*, 2012). A plot of (La/Sm)$_N$ against ^{87}Sr/^{86}Sr and ^{143}Nd/^{144}Nd ratios with data from assimilation and fractional crystallization (AFC) modeling between Ogol basalt, Tanzanian Craton granite–gneiss and Sadiman nephelinite suggests involvement of up to 5 % of nephelinitic component (Fig. 19). The combination of contamination with granite–gneisses and mixing with nephelinitic melts or contamination by unexposed Sadiman plutonic foiditic rocks can explain the observed geochemical characteristics. Involvement of nephelinite-type component is further supported by relatively high alkalinity ratios [molar (Na + K)/Al] of 0·98–1·07 of phonolitic glass and xenocrystic green core clinopyroxene (population IV) with perovskite and schorlomite (see above). At the same time, abundant xenocrysts (high-Fe olivine, diverse clinopyroxene cores and mantles, embayed plagioclase) suggest that mixing with other basaltic magmas is a further important process in evolution of the Ogol basalts.

Much of the compositional variation of the Ogol basalts (Fig. 4) can be explained by crystal fractionation processes and subsequent mixing between different melt batches related to fractionation of primary Ogol magma only. However, whole-rock data show that major and trace elements correlate with variable Sr and Nd isotope ratios (Figs 16 and 17). This is strong evidence against closed-system evolution of Ogol melts, because Sr and Nd isotopic ratios would not change during fractional crystallization under closed-system conditions. Although we cannot completely exclude that fractionation of primary Ogol magmas took place, our mineralogical and geochemical data suggest that magma mixing and mingling with melts related to the Lemagarut volcanic system is a more likely process. Rocks composing the Lemagarut volcano vary from relatively primitive basaltic rocks (Mg# = 58–56 and 537–495 ppm Cr) to highly evolved trachyandesite (Mg# = 27–30 and 15–3·4 ppm Cr) (Mollel, 2007). Our data show that the former contain olivine with compositions similar to Ogol phenocrysts with reverse zonation and the latter is rich in oligoclase–andesine$_{ss}$ phenocrysts. Diagrams showing relationships between major elements and isotopic ratios (Figs 16 and 17) support mixing between Ogol- and Lemagarut-derived melts.

The detailed relationships between Ogol and Lemagarut may be more complex. Although Hay (1987) assumed that Ogol lavas erupted from a series of individual vents, Mollel *et al.* (2011) provided some arguments in favor of a close genetic relation of Ogol and Lemagarut eruptions and suggested that Ogol basalts may represent distal flows from the Lemagarut volcano. Limited mineralogical data for the Lemagarut rocks (Mollel *et al.*, 2011) do not allow us to discuss possible genetic relations with Ogol rocks. At this stage we can only speculate that the volcanic series of Ogol and Lemagarut may record a uniform evolutionary history
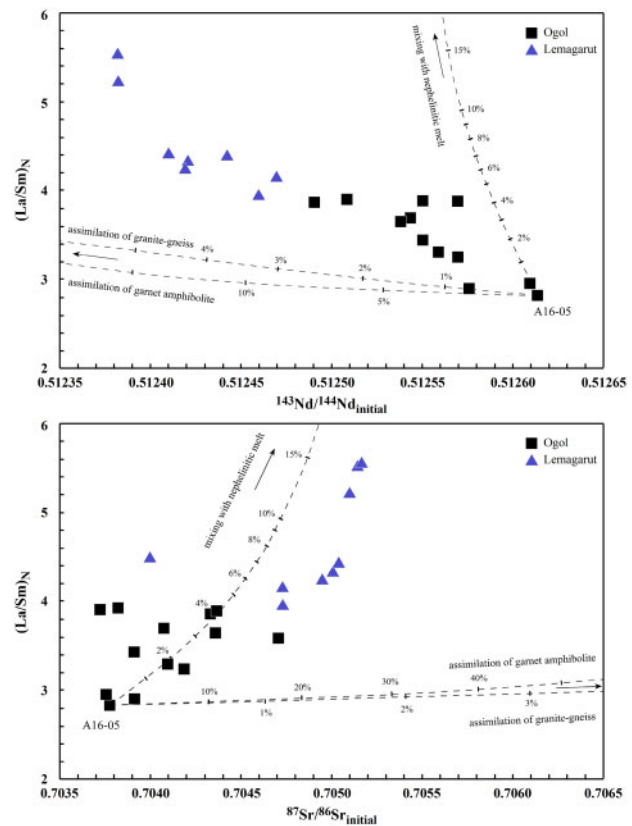

Fig. 19. Nd and Sr initial isotope rations vs (La/Sm)$_N$. Dashed lines show variations of the Ogol primitive basalt (A16-05) during fractional crystallization with crustal contamination of Precambrian granite–gneiss (A16-12), garnet amphibolite (A16-15c) or mixing with nephelinitic melt [sample Sad-10 from Zaitsev *et al.*, 2012; ^{87}Rb/^{86}Sr = 0·1071, ^{87}Sr/^{86}Sr = 0·705008(14) and ^{147}Sm/^{144}Nd = 0·0903, ^{143}Nd/^{144}Nd = 0·512511(3)]. The numbers show per cent of assimilation or mixing. AFC model; $R = 0.8$ (ratio of mass assimilation rate to the fractional crystallization rate).

reflected by the composition of a single parental melt and the onset of cotectic crystallization of olivine, pyroxene, magnetite and plagioclase. Linear correlations in major element abundances in Ogol and Lemagarut lavas are unlikely to reflect crystallization along a liquid line of descent. Simple AFC modelling indicates that Lemagarut derivatives could be the result of fractionation of 50–60 % Ogol melt with addition of 5 % crustal material. A detailed study of the Lemagarut volcano is needed to prove or disprove this idea.

CONCLUSIONS

The textural, mineralogical and geochemical heterogeneity of the Ogol basalts suggests that they formed under open-system conditions with magma hybridization as a major process. The formation and evolution of the Ogol basalts (Fig. 20) includes the following.

1. The formation of a primary Ogol melts occurred during partial melting of amphibole- (and phlogopite?) and garnet-bearing lithospheric material, as
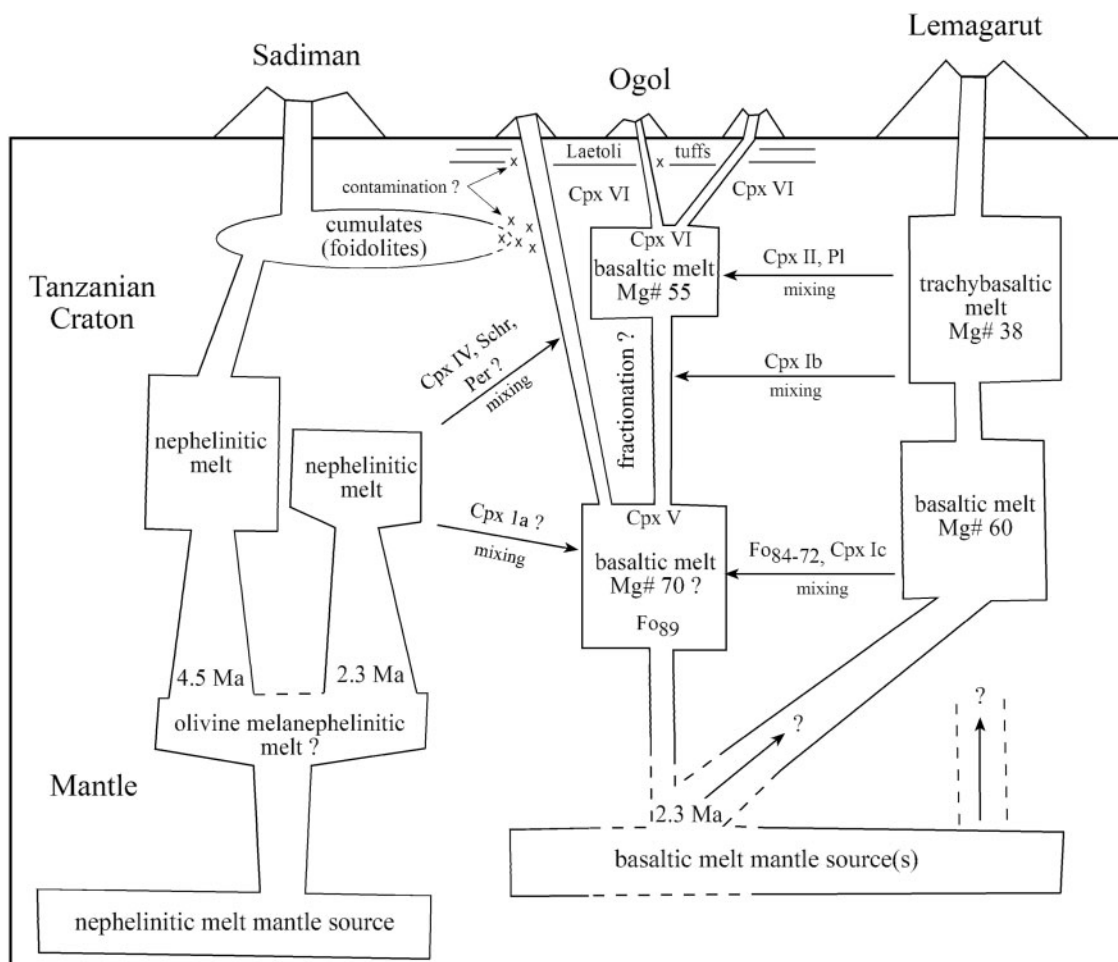
Fig. 20. Schematic diagram showing possible relationships between the magmatic plumbing systems of Ogol, Lemagarut and Sadiman.

suggested for some other volcanic complexes in the NTD (Mana *et al.*, 2015).

2. Although small degrees of fractional crystallization may explain the compositional variations of the studied samples, the presence of abundant xenocrysts (Fe-rich olivine with reverse zonation, clinopyroxene with variable composition, plagioclase) and variable Sr and Nd initial isotopic ratios suggest that magma mixing and mingling with other partly crystallized melts was important.

3. There is no clear evidence for a deep (mantle) origin of the various clinopyroxene xenocrysts. Early orthomagmatic augite (population V) crystallized at a temperature of ~1150–1220 °C, and an upper-crustal depth of 3–12 km (1–4 kbar). Late-stage augite (population VI) and magnetite–ulvöspinel$_{ss}$ are in textural equilibrium, whereas thermodynamic calculations indicate that groundmass olivine did not form contemporaneously.

4. (4) In particular, magma mixing and mingling between Ogol and Lemagarut melts can explain the observed mineralogical and chemical variations of the Ogol basalts. Magma mixing was not a single-stage process but happened at different depths with variable crystal residence times in melts during ascent to the surface.

5. Magma mixing and mingling with mantle-derived nephelinitic magma and/or contamination with foidolitic rocks crystallized beneath the Sadiman volcano or even from the melilite nephelinitic Laetolil tuffs did occur as indicated by the presence of green clinopyroxene, perovskite, schorlomite and titanite, but was a relatively minor process.

6. Small-scale contamination of the Ogol melts by crustal granite–gneises may have occurred. However, this assumption is based on geochemical modeling only, and no mineralogical evidence for this was found.

7. The Ogol basalts (particularly those from Oldoinyo Emusenge) seem to be the best examples of near-primary basaltic melts within the Crater Highlands region. They could also be considered as parental to the Lemagarut volcano, but more data are needed to solve this question.

ACKNOWLEDGEMENTS

SUPPLEMENTARY DATA

Supplementary data are available at *Journal of Petrology* online.

REFERENCES

Adams, A., Nyblade, A. & Weeraratne, D. (2012). Upper mantle shear wave velocity structure beneath the East African plateevidence for a deep, plateau wide low velocity anomaly. *Geophysical Journal International* **189**, 123–142.

Adelsberger, K. A., Wirth, K. R., Mabulla, A. Z. P. & Bowman, D. C. (2011). Geochemical and mineralogic characterization of Middle Stone Age tools of Laetoli, Tanzania, and comparisons with possible source materials. In: Harrison, T. (ed.) *Paleontology and Geology of Laetoli: Human Evolution in Context. Volume 1: Geology, Geochronology, Paleoecology and Paleoenvironment*. Dordrecht: Springer, pp. 143–166.

Andersen, D. J., Lindsley, D. H. & Davidson, P. M. (1993). QUILF–a Pascal program to assess equilibria among Fe–Mg–Mn–Ti oxides, pyroxenes, olivine, and quartz. *Computers & Geosciences* **19**, 1333–1350.

Aulbach, S., Rudnick, R. L. & McDonough, W. F. (2011). Evolution of the lithospheric mantle beneath the East African Rift in Tanzania and its potential signatures in rift magmas. In: Beccaluva, L., Bianchini, G. & Wilson, M. (eds) *Volcanism and Evolution of the African Lithosphere. Geological Society of America, Special Papers* **478**, 105–125.

Baker, B. H., Mohr, P. A. & Williams, L. A. J. (1972). *Geology of the Eastern Rift System of Africa*. Geological Society of America, Special Papers **136**, 1–68.

Bell, K. & Dawson, J. B. (1995). Nd and Sr isotope systematics of the active carbonatite volcano, Oldoinyo Lengai. In: Bell, K. & Keller, J. (eds) *Carbonatite Volcanism of Oldoinyo Lengai and Petrogenesis of Natrocarbonatite*. Berlin: Springer, pp. 100–112.

Bell, K. & Tilton, G. R. (2001). Nd, Pb and Sr isotopic compositions of East African carbonatites: evidence for mantle mixing and plume inhomogeneity. *Journal of Petrology* **42**, 1927–1945.

Birt, C. S., Maguire, P. K. H., Khan, M. A., Thybo, H., Keller, G. R. & Patel, J. (1997). The influence of pre-existing structures on the evolution of the southern Kenya Rift Valley — evidence from seismic and gravity studies. *Tectonophysics* **278**, 211–242.

Blundy, J. & Sparks, R. S. J. (1992). Petrogenesis of mafic enclaves in granitoids of the Adamello massif. *Journal of Petrology* **33**, 1039–1104.

Bradshaw, R. W., Kent, A. J. R. & Tepley III, F. J. (2018). Chemical fingerprints and residence times of olivine in the 1959 Kilauea Iki eruption, Hawaii: Insights into picrite formation. *American Mineralogist* **103**, 1812–1826.

Braunger, S., Marks, M. A. W., Wenzel, T., Zaitsev, A. N. & Markl, G. (2021). The petrology of the Tarosero volcanic complex: constraints on the formation of extrusive agpaitic rocks. *Journal of Petrology* **62**, 10.1093/petrology/egab015

Carmichael, I. S., Frey, H. M., Lange, R. A. & Hall, C. M. (2006). The Pleistocene cinder cones surrounding Volcán Colima, Mexico re-visited: eruption ages and volumes, oxidation states, and sulfur content. *Bulletin of Volcanology* **68**, 407–419.

Church, A. A. (1995). The petrology of the Kerimasi carbonatite volcano and the carbonatites of Oldoinyo Lengai with a review of other occurrences of extrusive carbonatites. PhD thesis. Natural History Museum. London.

Clarke, L. B. & Le Bas, J. M. (1990). Magma mixing and metasomatic reaction in silicate–carbonate liquids at the Kruidfontein carbonatitic volcanic complex. *Mineralogical Magazine* **54**, 45–56.

Corsaro, R. A., Métrich, N., Allard, P., Andronico, D., Miraglia, L. & Fourmentraux, C. (2009). The 1974 flank eruption of Mount Etna: an archetype for deep dike-fed eruptions at basaltic volcanoes and a milestone in Etna's recent history. *Journal of Geophysical Research* **114**, B07204.

Dawson, J. B. (2002). Metasomatism and partial melting in upper-mantle peridotite xenoliths from the Lashaine volcano, northern Tanzania. *Journal of Petrology* **43**, 1749–1777.

Dawson, J. B. (2008). The Gregory Rift Valley and Neogene–recent volcanoes of Northern Tanzania. Geological Society Memoir No. 33, Geological Society, London, 102 p.

Dawson, J. B. & Smith, J. V. (1988). Metasomatised and veined upper-mantle xenoliths from Pello Hill, Tanzania: evidence for anomalously-light mantle beneath the East African Rift Valley. *Contributions to Mineralogy and Petrology* **100**, 510–527.

Deino, A. L. (2011). ^{40}Ar/^{39}Ar dating of Laetoli, Tanzania. In: Harrison, T. (ed.) *Paleontology and Geology of Laetoli: Human Evolution in Context. Volume 1: Geology, Geochronology, Paleoecology and Paleoenvironment*. Dordrecht: Springer, pp. 77–97.

Deino, A. L. (2012). ^{40}Ar/^{39}Ar dating of Bed I, Olduvai Gorge, Tanzania, and the chronology of early Pleistocene climate change. *Journal of Human Evolution* **63**, 251–273.

Dobosi, G. (1989). Clinopyroxene zoning patterns in the young alkali basalts of Hungary and their petrogenetic significance. *Contributions to Mineralogy and Petrology* **101**, 112–121.

Dobosi, G. & Fodor, R. V. (1992). Magma fractionation, replenishment, and mixing as inferred from green-core clinopyroxenes in Pliocene basanite, southern Slovakia. *Lithos* **28**, 133–150.

Duda, A. & Schmincke, H.-U. (1985). Polybaric differentiation of alkali basaltic magmas: evidence from green-core clinopyroxenes (Eifel, FRG). *Contributions to Mineralogy and Petrology* **91**, 340–353.

Fletcher, A. W., Abdelsalam, M. G., Emishaw, L., Atekwana, E. A., Laó-Dávila, D. A. & Ismail, A. (2018). Lithospheric controls on the rifting of the Tanzanian Craton at the Eyasi Basin. *Tectonics* **37**, 2818–2815.

Foster, A., Ebinger, C., Mbede, E. & Rex, D. (1997). Tectonic development of the northern sector of the East African Rift System. *Journal of the Geological Society, London* **154**, 689–700.

Furman, T., Kaleta, K. M., Bryce, J. G. & Hanan, B. B. (2006). Tertiary mafic lavas of Turkana, Kenya: constraints on the East African plume structure and the occurrence of high-μ volcanism in Africa. *Journal of Petrology* **47**, 1221–1244.

Hart, S. R., Hauri, E. H., Oschmann, L. A. & Whitehead, J. A. (1992). Mantle plumes and entrainment: isotopic evidence. *Science* **256**, 517–520.

Hay, R. L. (1987). Geology of the Laetoli Area. In: Leakey, M. D. & Harris, J. M. (eds) *Laetoli: A Pliocene Site in Northern Tanzania*. Oxford: Clarendon Press, pp. 23–47.

Hill, R. & Roeder, P. (1974). The crystallization of spinel from basaltic liquid as a function of oxygen fugacity. *Journal of Geology* **82**, 709–729.

Jankovics, M. É., Taracsák, Z., Dobosi, G., Embey-Isztin, A., Batki, A., Harangi, S. & Hauzenberger, C. A. (2016). Clinopyroxene with diverse origins in alkaline basalts from the western Pannonian Basin: implications from trace element characteristics. *Lithos* **262**, 120–134.

Jerram, D. A. & Martin, V. M. (2008). Understanding crystal populations and their significance through the magma plumbing system. In: Annen, C. & Zellmer, G.F. (eds) *Dynamics of Crustal Magma Transfer, Storage and Differentiation. Geological Society, Londom, Special Publications* **304**, 133–148.

Johnson, L. H., Jones, A. P., Church, A. A. & Taylor, W. R. (1997). Ultramafic xenoliths and megacrysts from a melilitite tuff cone, Deeti, northern Tanzania. *Journal of African Earth Sciences* **25**, 29–42.

Keller, J., Zaitsev, A. N. & Wiedenmann, D. (2006). Primary magmas at Oldoinyo Lengai: the role of olivine melilitites. *Lithos* **91**, 150–172.

Kokfelt, T. F., Weatherley, S. M., Keiding, J. K. & Árting, T. B. (2015). Magma mixing, mingling and hybridisation at different crustal levels: snapshots from 1·9 billion years of magmatism in south-eastern Greenland. *Geological Survey of Denmark and Greenland Bulletin* **33**, 45–48.

Koornneef, J. M., Davies, G. R., Döpp, S. P., Vukmanovic, Z., Nikogosian, I. K. & Mason, P. R. D. (2009). Nature and timing of multiple metasomatic events in the sub-cratonic lithosphere beneath Labait, Tanzania. *Lithos* **112S**, 896–912.

Leakey, M. D. & Hay, R. L. (1979). Pliocene footprints in the Laetolil Beds at Laetoli, northern Tanzania. *Nature* **278**, 317–323.

Le Bas, M. J. L., Le Maitre, R. W., Streckeisen, A., Zanettin, B. & IUGS Subcommission on the Systematics of Igneous Rocks (1986). A chemical classification of volcanic rocks based on the total alkali–silica diagram. *Journal of Petrology* **27**, 745–750.

Le Gall, B., Nonnotte, P., Rolet, J., Benoit, M., Guillou, H., Mousseau-Nonnotte, M., Albaric, J. & Deverchère, J. (2008). Rift propagation at craton margin. Distribution of faulting and volcanism in the North Tanzanian Divergence (East Africa) during Neogene times. *Tectonophysics* **448**, 1–19.

Li, C., Thakurta, J. & Ripley, E. M. (2012). Low-Ca contents and kink-banded textures are not unique to mantle olivine: evidence from the Duke Island Complex, Alaska. *Mineralogy and Petrology* **104**, 147–153.

Mana, S., Furman, T., Carr, M. J., Mollel, G. F., Mortlock, R. A., Feigenson, M. D., Turrin, B. D. & Swisher, I. I C. C. (2012). Geochronology and geochemistry of the Essimingor volcano: melting of metasomatized lithospheric mantle beneath the North Tanzanian Divergence zone (East African Rift). *Lithos* **155**, 310–325.

Mana, S., Furman, T., Turrin, B. D., Feigenson, M. D. & Swisher, C. C. (2015). Magmatic activity across the East African North Tanzanian Divergence Zone. *Journal of the Geological Society, London* **172**, 368–389.

Manega, P. C. (1993). *Geochronology, geochemistry and isotope study of the Plio-Pleistocene hominid sites and the Ngorongoro Volcanic Highlands in Northern Tanzania*. PhD thesis, Boulder: University of Colorado.

Mangler, M. F., Petrone, C. M., Hill, S., Delgado-Granados, H. & Prytulak, J. (2020). A pyroxenic view on magma hybridization and crystallization at Popocatépetl volcano, Mexico. *Fronties in Earth Sciences* **8**, 362.

Mattsson, H. B., Nandedkar, R. H. & Ulmer, P. (2013). Petrogenesis of the melilititic and nephelinitic rock suites in the Lake Natron–Engaruka monogenetic volcanic field, northern Tanzania. *Lithos* **179**, 175–192.

Mitchell, R. H. (1972). Composition of perovskite in kimberlite. *American Mineralogist* **57**, 1748–1753.

Mollel, G. F. (2007). *Petrochemistry and Geochronology of Ngorongoro Volcanic Highland Complex (NVHC) and Its Relationship to Laetoli and Olduvai Gorge, Tanzania*. PhD thesis, Rutgers University, New Brunswick, NJ.

Mollel, G. F., Swisher, C. C., III, Feigenson, M. D., & Carr, M. J. (2008). Geochemical evolution of Ngorongoro Caldera, Tanzania: implications for crust–magma interaction. *Earth and Planetary Science Letters* **271**, 337–347.

Mollel, G. F., Swisher, C. C., III, Feigenson, M. D. & Carr, M. J. (2011). Petrology, Geochemistry, and Age of Satiman, Lemagurut and Oldeani: sources of the Volcanic Deposits of the Laetoli Area. In: Harrison, T. (ed.) *Paleontology and Geology of Laetoli: Human Evolution in Context. Volume 1: Geology, Geochronology, Paleoecology and Paleoenvironment*. Dordrecht: Springer, pp. 99–120.

Morgavi, D., Arienzo, I., Montagna, C., Perugini, D. & Dingwell, D. B. (2019). Magma mixing: history and dynamics of an Eruption Trigger. In: Gottsmann, J., Neuberg, J. & Scheu, B. (eds) *Volcanic Unrest—From Science to Society*. Cham, Switzerland: Springer, pp. 123–137.

Neave, D. A. & Putirka, K. D. (2017). A new clinopyroxene–liquid barometer, and implications for magma storage pressures under Icelandic rift zones. *American Mineralogist* **102**, 777–794.

Nelson, S. T. & Montana, A. (1992). Sieve-textured plagioclase in volcanic rocks produced by rapid decompression. *American Mineralogist* **77**, 1242–1249.

Nimis, P. & Ulmer, P. (1998). Clinopyroxene geobarometry of magmatic rocks Part 1: An expanded structural geobarometer for anhydrous and hydrous, basic and ultrabasic systems. *Contributions to Mineralogy and Petrology* **133**, 122–135.

Nonnotte, P. (2007). *Etude Volcano-Tectonique de la Zone de Divergence Nord Tanzanienne (Terminaison Sud du Rift Kenyan). Caractérisation Pétrologique et Géochimique du Volcanisme Récent (8 Ma–Actuel) et du Manteau Source*. Doctorat These, Université de Bretagne Occidentale, Brest.

Nonnotte, P., Guillou, H., Le Gall, B., Benoit, M., Cotten, J. & Scaillet, S. (2008). New K–Ar age determinations of Kilimanjaro volcano in the North Tanzanian diverging rift. *Journal of Volcanology and Geothermal Research* **173**, 99–112.

Paslick, C., Halliday, A. N., James, D. & Dawson, J. B. (1995). Enrichment of continental lithosphere by OIB melts: isotopic evidence from the volcanic province of northern Tanzania. *Earth and Planetary Science Letters* **130**, 109–126.

Paslick, C. R., Halliday, A. N., Lange, R. A., James, D. & Dawson, J. B. (1996). Indirect crustal contamination: evidence from isotopic and chemical disequilibria in minerals from alkali

basalts and nephelinites from northern Tanzania. *Contributions to Mineralogy and Petrology* **125**, 277–292.

Peirce, S. & Mana, S. (2018). Fractional crystallization history recorded by the lava flows of Ketumbeine volcano, North Tanzania. *Geological Society of America, Abstracts with Programs* **50**, 10.1130/abs/2018NE-311204

Perugini, D. & Poli, G. (2012). The mixing of magmas in plutonic and volcanic environments: analogies and differences. *Lithos* **153**, 261–277.

Petrone, C. M. (2010). Relationship between monogenetic magmatism and stratovolcanoes in western Mexico: the role of low-pressure magmatic processes. *Lithos* **119**, 585–606.

Pickering, R. (1964). *Endulen. Quarter Degree Sheet 52*. Dodoma: Tanzania Geological Survey.

Plasman, M., Hautot, S., Tarits, P., Gautier, S., Tiberi, C., Le Gall, B., Mtelela, K. & Gama, R. (2019). Lithospheric structure of a transitional magmatic to amagmatic continental rift system—insights from magnetotelluric and local tomography studies in the North Tanzanian Divergence. *Geosciences* **9**, 462.

Putirka, K. D. (2008). Thermometers and barometers for volcanic systems. In: Putirka, K., Tepley, F. (eds.), *Mineralogical Society of America and Geochemical Society, Reviews in Mineralogy and Geochemistry* **69**, 61–120.

Putirka, K., Johnson, M., Kinzler, R., Longhi, J. & Walker, D. (1996). Thermobarometry of mafic igneous rocks based on clinopyroxene–liquid equilibria, 0–30 kbar. *Contributions to Mineralogy and Petrology* **123**, 92–108.

Reubi, O., Nicholls, I. A. & Kamenetsky, V. S. (2002). Early mixing and mingling in the evolution of basaltic magmas: evidence from phenocryst assemblages, Slamet Volcano, Java, Indonesia. *Journal of Volcanology and Geothermal Research* **119**, 255–274.

Ritsema, J., Nyblade, A. A., Owens, T. J., Langston, C. A. & VanDecar, J. C. (1998). Upper mantle seismic velocity structure beneath Tanzania, east Africa: implications for the stability of cratonic lithosphere. *Journal of Geophysical Research: Solid Earth* **103**, 21201–21213.

Rogers, N. W., Macdonald, R., Fitton, J. G., George, R., Smith, M. & Barreiro, B. (2000). Two mantle plumes beneath the East African Rift system: Sr, Nd, and Pb isotope evidence from Kenya Rift basalts. *Earth and Planetary Science Letters* **176**, 387–400.

Rooney, T. O. (2017). The Cenozoic magmatism of East Africa: Part I—flood basalts and pulsed magmatism. *Lithos* **286–287**, 264–301.

Rooney, T. O. (2020a). The Cenozoic magmatism of East Africa: Part II—rifting of the mobile belt. *Lithos* **360–361**, 105291.

Rooney, T. O. (2020b). The Cenozoic magmatism of East Africa: Part III—rifting of the craton. *Lithos* **360–361**, 105390.

Rooney, T. O. (2020c). The Cenozoic magmatism of East Africa: Part IV—The terminal stages of rifting preserved in the Northern East African Rift System. *Lithos* **360–361**, 105381.

Rooney, T. O. (2020d). The Cenozoic magmatism of East Africa: Part V—Magma sources and processes in the East African Rift. *Lithos* **360–361**, 105296.

Shane, P., Cocker, K., Coote, A., Stirling, C. H. & Reid, M. R. (2019). The prevalence of plagioclase antecrysts and xenocrysts in andesite magma, exemplified by lavas of the Tongariro volcanic complex, New Zealand. *Contributions to Mineralogy and Petrology* **174**, 89.

Simkin, T. & Smith, J. V. (1970). Minor-element distribution in olivine. *The Journal of Geology* **78**, 304–325.

Simonetti, A. & Bell, K. (1993). Isotopic disequilibrium in clinopyroxenes from nephelinitic lavas, Napak volcano, eastern Uganda. *Geology* **21**, 243–246.

Simonetti, A., Shore, M. & Bell, K. (1996). Diopside phenocrysts from nephelinite lavas, Napak volcano, Eastern Uganda: Evidence for magma mixing. *Canadian Mineralogist* **34**, 411–421.

Smith, M. (1994). Stratigraphic and structural constraints on mechanisms of active rifting in the Gregory Rift. *Tectonophysics* **236**, 3–22.

Sparks, R. S. J. & Marshall, L. A. (1986). Thermal and mechanical constraints on mixing between mafic and silicic magmas. *Journal of Volcanology and Geothermal Research* **29**, 99–124.

Stewart, M. L. & Pearce, T. (2004). Sieve-textured plagioclase in dacitic magma: interference imaging results. *American Mineralogist* **89**, 348–351.

Sun, S.-S. & McDonough, W. F. (1989). Chemical and isotopic systematics of oceanic basalts: implications for mantle composition and processes. In: Saunders, A. D. & Norry, M. J. (eds) *Magmatism in the Ocean Basins.Geological Society, London, Special Publications* **42**, 313–345.

Sundermeyer, C., Gätjen, J., Weimann, L. & Wörner, G. (2020). Timescales from magma mixing to eruption in alkaline volcanism in the Eifel volcanic fields, western Germany. *Contributions to Mineralogy and Petrology* **175**, 77.

Svetov, S. A., Stepanova, A. V., Chazhengina, S. Yu., , Svetova, E. N., Rybnikova, Z. P., Mikhailova, A. I., Paramonov, A. S., Utitsyna, V. L., Ekhova, M. V. & Kolodey, B. S. (2015). Precision geochemical (ICP-MS, LA-ICP-MS) analysis of rock and mineral compositions: the method and accuracy estimation in the case study of Early Precambrian mafic complexes. *Proceedings of Karelian Research Centre of RAS* **7**, 54–73.

Tao, Y., Putirka, K., Hu, R.-Z. & Li, C. (2015). The magma plumbing system of the Emeishan large igneous province and its role in basaltic magma differentiation in a continental setting. *American Mineralogist* **100**, 2509–2517.

Ubide, T., Galé, C., Larrea, P., Arranz, E. & Lago, M. (2014). Antecrysts and their effect on rock compositions: the Cretaceous lamprophyre suite in the Catalonian Coastal Ranges (NE Spain). *Lithos* **206–207**, 214–233.

Ulmer, P. (1989). The dependence of the Fe^{2+}–Mg cation-partitioning between olivine and basaltic liquid on pressure, temperature and composition. An experimental study to 30 kbars. *Contributions to Mineralogy and Petrology* **101**, 261–273.

Vasil'eva, I. E. & Shabanova, E. V. (2017a). *Catalogue of Certified Reference Materials of Natural and Man-Made Media Compositions*. Irkutsk: A. P. Vinogradov Institute of Geochemistry SB RAS, 79 pp.

Vasil'eva, I. E. & Shabanova, E. V. (2017b). Certified reference materials of geological and environmental objects: problems and solutions. *Journal of Analytical Chemistry* **72**, 129–146.

Vladimirov, A. G., Mekhonoshin, A. S., Khromykh, S. V., Mikheev, E. I., Travin, A. V., Volkova, N. I., Kolotilina, T. B., Davidenko, Yu. A., Borodina, E. V. & Khlestov, V. V. (2017). Mechanisms of mantle–crust interaction at deep levels of collision orogens (case of the Olkhon region, West Pribaikalie). *Geodynamics & Tectonophysics* **8**, 223–268.

Wang, K., Plank, T., Walker, J. D. & Smith, E. I. (2002). A mantle melting profile across the Basin and Range, SW USA. *Journal of Geophysical Research* **107**, 2017.

Zaitsev, A. N., Wenzel, T., Spratt, J., Williams, T. C., Strekopytov, S., Sharygin, V. V., Petrov, S. V., Golovina, T. A., Zaitseva, E. O. & Markl, G. (2011). Was Sadiman volcano a source for the Laetoli Footprint Tuff? *Journal of Human Evolution* **61**, 121–124.

Zaitsev, A. N., Marks, M. A. W., Wenzel, T., Spratt, J., Sharygin, V. V., Strekopytov, S. & Markl, G. (2012). Mineralogy, geochemistry and petrology of the phonolitic to nephelinitic

Sadiman volcano, Crater Highlands, Tanzania. *Lithos* **152**, 66–83.

Zaitsev, A. N., Avdontseva, E.Yu, Britvin, S. N., Demeny, A., Homonnay, Z., Jeffries, T. E., Keller, J., Krivovichev, V. G., Markl, G., Platonova, N. V., Siidra, O. I., Spratt, J. & Vennemann, T. (2013). Oxo-magnesio-hastingsite, $NaCa_2(Mg_2Fe^{3+})(Al_2Si_6)O_{22}O_2$, a new anhydrous amphibole from the Deeti volcanic cone, Gregory rift, northern Tanzania. *Mineralogical Magazine* **77**, 2773–2792.

Zaitsev, A. N., Spratt, J., Sharygin, V. V., Wenzel, T., Zaitseva, O. A. & Markl, G. (2015). Mineralogy of the Laetolil footprint tuff: a comparison with possible volcanic sources from the Crater Highlands and Gregory rift. *Journal of African Earth Sciences* **111**, 214–221.

Zaitsev, A. N., McHenry, L., Savchenok, A. I., Strekopytov, S., Spratt, J., Humphreys-Williams, E., Sharygin, V. V., Bogomolov, E. S., Chakhmouradian, A. R., Zaitseva, O. A., Arzamastsev, A. A., Reguir, E. P., Leach, L., Leach, M. & Mwankunda, J. (2019). Stratigraphy, mineralogy and geochemistry of the Upper Laetolil tuffs including a new Tuff 7 site with footprints of *Australopithecus afarensis*, Laetoli, Tanzania. *Journal of African Earth Sciences* **158**, 103561.